SENSITIVITY OF THE MUELLER MATRIX TO THE OPTICAL AND MICROPHYSICAL PROPERTIES OF CIRRUS CLOUDS

A Thesis

by

RYAN LEE LAWLESS

Submitted to the Office of Graduate Studies of
Texas A&M University
in partial fulfillment of the requirements for the degree of

MASTER OF SCIENCE

August 2005

Major Subject: Atmospheric Sciences

SENSITIVITY OF THE MUELLER MATRIX TO THE OPTICAL AND MICROPHYSICAL PROPERTIES OF CIRRUS CLOUDS

A Thesis

by

RYAN LEE LAWLESS

Submitted to the Office of Graduate Studies of
Texas A&M University
in partial fulfillment of the requirements for the degree of

MASTER OF SCIENCE

Approved by:

Chair of Committee,	Ping Yang
Committee Members,	George W. Kattawar
	Thomas Wilheit
	Jerry R. North
Head of Department,	Richard Orville

August 2005

Major Subject: Atmospheric Sciences

ABSTRACT

Sensitivity of the Mueller Matrix to the Optical and Microphysical Properties of Cirrus Clouds. (August 2005)

Ryan Lee Lawless, B.S., Texas A&M University

Chair of Advisory Committee: Dr. Ping Yang

An adding-doubling method is employed to calculate the reflected Stokes parameters for cirrus cloud layers composed of different habits and effective sizes. The elements of the Mueller matrix are determined from the reflected Stokes parameters by considering four different incident polarization states. The sensitivity of these elements is observed by comparing different ice crystal habits, effective sizes, and optical depth. The Mueller elements are strongly dependent on habit. The three habits, aggregate, bullet rosette, and plate, are observed and the M_{12}/M_{11}, M_{43}/M_{11} and M_{44}/M_{11} elements are discussed. The wavelength used is $\lambda = 0.532 \mu m$, which is the lidar wavelength used on the CALIPSO satellite. The linear depolarization ratio is also discussed. The method of subtracting the two depolarization ratios, $\delta_h - \delta_v$, is noted as another way to possibly better distinguish ice crystal habits.

The sensitivity of the Mueller matrix to effective size is also observed. For three size distributions, the Mueller elements indicate no strong dependence. This may be due to the assumption of randomly oriented ice. Also, using an absorbing wavelength might provide dependence. Finally, the Mueller elements are dependent on optical depth. For a greater optical depth, the strength of reflection increases while the polarization decreases. As the optical depth increases, any peak-like features become non-existent.

DEDICATION

To my family, most especially, my wife, Jessica

ACKNOWLEDGEMENTS

I would particularly like to thank, Dr. Ping Yang. He has shown faith in me by supporting me in graduate school and allowing me to pursue this most interesting work. I would further like to thank the rest of my committee members for being a part of this effort. Particularly, I would like to thank Dr. Kattawar for his guidance. Dr. Johan de Haan provided me with the radiative transfer code I used in my research. I must thank him for this tool and for his assistance with all my problems during this process.

I also must thank all the wonderful people that work so hard in the twelfth floor office. More specifically, Mrs. Pat Price has been an amazing help. Her advice and support have strongly influenced my decisions. Thank you to all my fellow graduate students. I would like to acknowledge Zhibo Zhang for all our numerous discussions. They have been quite beneficial to this learning process. Not only have I expanded my knowledge in this field, but I also have gained a new friend.

Thank you to all my friends and family. My parents have given me love and support during my entire college career. My mom, in particular, has continually given me all the necessary encouragement. To my step-grandparents, who have always provided me a place to live: thank you so much. Finally, my wife, Jessica, has given me so much to love. She is my motivation to be a better person and to grow closer to God.

Finally, the research reported in this thesis was partially supported by grants from the National Science Foundation (ATM-458131), the NASA Radiation Sciences Program (NAG-1-02002), and a subcontract (4400053274) from Science Applications International Corporation. The reported results herein do not necessarily reflect the views of these agencies.

TABLE OF CONTENTS

LIST OF FIGURES

FIGURE Page

LIST OF TABLES

CHAPTER I

INTRODUCTION AND HISTORY

Cirrus clouds are spatially abundant and temporally persistent across the Earth. Despite their abundance and the avid determination to define their properties, the total influence and range of their radiative forcing is not well identified.[1,2,3] The lack of knowledge about cirrus clouds is attributed to the vast range of cirrus cloud properties, both macro-physical and microphysical, and their uncertainty.[4] One step in this direction, is to use radiative transfer to gain information about cirrus clouds. The reflected and transmitted beam due to interaction with the cirrus cloud is dependent on the cirrus cloud properties. By using the intensity and polarization of light and a radiative transfer model, the Mueller matrix is determined. The Mueller matrix offers 15 more opportunities, compared to the intensity, to focus in on the constituents of the cirrus cloud. In this study, the Mueller matrix is analyzed to understand its dependence on cirrus cloud properties.

Single-Scattering Properties

The single-scattering properties for a population of ice crystals are needed to calculate the radiative properties of a cirrus cloud layer. To calculate the single-scattering properties for a population of cirrus clouds, specific size distributions and habit distributions are required. These are obtained by field experiments.

It has been shown that the ice crystals that form cirrus clouds are non-spherical[5] and in the middle latitudes consist mainly of bullet rosettes, aggregates, hollow columns, and plates.[6,7,8] The First International Satellite Cloud Climatology Project (ISCCP)

This thesis follows the style of Applied Optics.

Regional Experiment (FIRE) helped confirm the abundance of these specific habits in the middle latitudes, and along with the Atmospheric Radiation Measurement (ARM) program, increased our understanding of cirrus microphysical and radiative properties at a local level.[9,10] A true representation of cirrus clouds requires complete experimental coverage across the entire Earth, which is not currently possible. Heymsfield[11] used aircraft measurements to determine that cirrus clouds are highly variable in size and shape.

Twenty-one size distributions were taken from various experiments for the middle latitudes. Included are those from Heymsfield[11] for cirrostratus and cirrus uncinus. Also, size distributions from Heymsfield and Platt[6] are used: two distributions for modified warm and cold cirrus clouds, and the rest determined at various temperature ranges in the atmosphere. Size distributions also come from the more recent and intense two phase FIRE campaign: FIRE I and FIRE II. FIRE II used instruments able to collect data for ice crystals as small as 10 μm. FIRE I, used two probes to observe ice crystals from 25 μm to above 2000 μm.[9] Fu[12] used all these size distributions to calculate the single-scattering properties using a ray-tracing technique. Finally, the last two sets considered come from Mitchell et al.[13]

A habit distribution is used to determine the average and bulk scattering properties for a sample of ice crystals composed of different habits. Although, field campaigns (FIRE I and II, ARM, etc.) have done an extensive job observing ice crystal habits in cirrus clouds, detailed information regarding habit distribution and habit percentage per size distribution is still unavailable. Despite the lack of habit information, habit percentages based on data collected during FIRE II were used in to calculate the

average and bulk properties in Baum et al.[14] Those same percentages will be used in this research for a mixed habit ice cloud. The four most common habits found in cirrus clouds, aggregate, bullet rosette, plate, and hollow column, are used in these scattering models.

Although, there are many methods specifically developed to describe the scattering of light through an ice crystal,[15,16,17] modeling the single-scattering properties of ice crystals is nonetheless quite difficult and often time consuming. Currently, there is not an exact solution for light scattering by non-spherical ice crystals that cover all shapes and sizes.[18]

In the first scattering calculations, Mie scattering was considered to describe radiative interactions. The Lorenz-Mie theory exactly explains the scattering of a spherical particle. However, the field experiments, noted above, concluded that this theory inadequately describes the scattering properties of ice crystals.[12] Also, Takano and Liou[19] previously recognized that the Lorenz-Mie theory was inapplicable to the optical phenomena produced by hexagonal ice crystals.

Cai and Liou[15] developed the conventional geometric ray tracing technique, including polarization, for randomly oriented hexagonal ice crystals. The total electric field vector was determined by adding the outgoing electric fields in the same direction. Takano and Liou[19] extended this ray tracing technique to include ice crystal size distributions, birefringence, and a proper treatment of the δ-function transmission. Yang and Liou[17] further refined the conventional method to appropriately model the extinction efficiency. Two of their methods were also compared: finite difference time domain and a geometric optics code. The Improved Geometric Optics Method (IGOM) is found to

compare well with FDTD for size parameters larger than 20 μm. IGOM is based on ray tracing, and only approximately calculates the surface field. Because of its relatively good results and availability, IGOM is used to construct the single-scattering properties for randomly oriented ice crystals in a cirrus cloud.

Radiative Transfer History

In the early 20th century, astrophysicists worked on the subject of radiative transfer in stellar media. Chandrasekhar[20] extended radiative transfer to plane-parallel systems and specifically determined the exact solution, including polarization, for Rayleigh scattering. Coulson et al.[21] used Chandrasekhar's formulation of radiative transfer for Rayleigh scattering to calculate the Stokes vectors for the diffuse reflected and transmitted radiation, i.e. the diffuse upward and downward radiation. van de Hulst[22] worked through the reflection and transmission functions, which can be applied to the radiative transfer problem. The adding-doubling method[23] calculates the reflection and transmission matrices to determine the scattered polarized radiation due to plane-parallel layers.

Polarization

In the paper by Stokes,[24] the polarization of light was presented as a set of values known today as Stokes parameters. The Stokes parameters are additive so long as no permanent phase relationships between the individual beams hold; therefore, the beams are incoherent. This is crucial to the use of the Stokes parameters, because the total intensity and polarization in a given direction due to different beams, i.e. multiple scattering, can be added together.

Chandrasekhar[25] first included the Stokes parameters in the radiative transfer problem. The radiative transfer equation, including the vector representation of light, is the vector radiative transfer equation (VRTE), which the Stokes parameters are a solution. The inclusion of polarization is necessary to accurately determine the interaction of radiation with a medium and to possibly gain more information about that medium.

Lenoble[26] gives brief explanations of many methods, both scalar and vector, for solving the radiative transfer problem. Plass and Kattawar[27] used a Monte Carlo approach to calculate the scattering of visible light through a horizontally stratified water cloud. Multiple scattering and an anisotropic scattering function are taken into account. Takano and Liou[19] applied the adding-doubling method to calculate reflected and transmitted intensities and polarization for randomly and horizontally oriented ice crystals. In this study, an adding-doubling method[23] is used to model the reflected radiation field due to a cirrus cloud layer. This method can calculate the scattered Stokes parameters.

CHAPTER II

RADIATIVE TRANSFER

The concept of radiative transfer can be applied to any absorbing, emitting and/or scattering medium. The radiation field that is induced by the interaction of some incident radiation with a medium is determined by solving the radiative transfer problem. Information about the medium is contained in the induced radiation field, which is particularly useful to remote sensing.

Electromagnetic radiation can propagate through almost any medium and unlike sound waves; it can propagate in a vacuum. As radiation propagates through a medium, interactions occur between the incident radiation beam and the constituents of the medium. For instance, both scattering and absorption can take place, weakening the incident beam. Scattering redirects some fraction of the incident radiation in to all other directions according to the properties of the medium. Absorption, or "true absorption" from Chandrasekhar,[20] is the process that removes some other fraction of the incident beam and transforms that energy into other energy forms or into energy at other frequencies.

Equations

Consider a volume element with thickness ds and cross sectional area dA. The amount of incident intensity, I_λ, is weakened as it traverses the volume element. As shown in Fig. 1, the outgoing intensity becomes the incident intensity plus some change in the intensity, dI_λ, due to the medium. The subscript λ indicates monochromatic radiation.

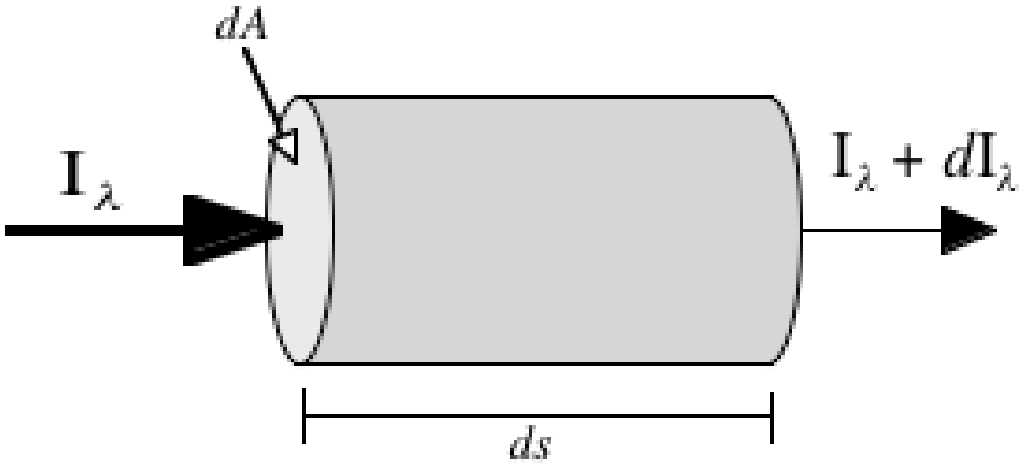

Fig. 1. Energy Incident on a Volume Element. This simplified model shows the very basic idea of the medium removing energy from the incident direction.

The change in intensity depends on the thickness, ds, density, ρ, and the mass extinction coefficient, $\kappa_{e\lambda}$, of the volume element. The mass extinction coefficient denotes the amount of energy removed from the incident beam per mass of the volume element ($cm^2\ g^{-1}$). Here, extinction of the energy is due to scattering and absorption. The change in energy of the radiation beam traversing the volume element is defined[28] as

$$dE_\lambda = -\kappa_{e\lambda}\,\rho\,I_\lambda\cos\theta\,ds\,d\lambda\,dA\,d\omega\,dt\,. \tag{1}$$

It is dependent on the incident intensity, I_λ, defined as the energy per wavelength per time per area perpendicular to the direction of propagation per steradian. In radiative transfer, the radiation is confined to a pencil of radiation, so the solid angle, $d\omega$, indicates the intensity is dependent on direction. The energy is in the specified

wavelength interval, λ to $\lambda + d\lambda$. For the case where the incident energy is not perpendicular to the surface, dA, the cosine of the angle θ from the perpendicular is included, as in Eq. (1).

Now, the extinction of radiation due to scattering will be regarded. Eq. (1) is formulated to include the phase function, $\mathrm{P}(\cos\Theta)$, which describes the angular distribution of scattered energy. The amount of energy scattered at an angle, Θ, from the incident direction and into a solid angle, $d\Omega$, is expressed by

$$d\mathrm{E}_\lambda = -\kappa_{s\lambda}\,\mathrm{I}_\lambda \frac{\mathrm{P}(\cos\Theta)d\Omega}{4\pi} dm\, d\lambda\, d\omega\, dt \,, \tag{2}$$

where the scattering coefficient $\kappa_{s\lambda}$, due to scattering only, has the same units as the extinction coefficient. The differential mass, $dm = \rho ds dA$. Figure 2, similar to Tynes,[28] depicts a pencil of radiation traversing a volume element, which is incident at some angle θ to the surface dA and is scattered into the direction $d\Omega$.

Energy may also be gained in a specified direction. The processes that contribute to an increase in energy are the emission of radiation by the constituents of the medium and the scattering from all other directions of the medium at the same wavelength into the solid angle of interest. The change in energy due to emission is

$$d\mathrm{E}_\lambda = j_\lambda\, dm\, d\lambda d\omega\, dt \,, \tag{3}$$

such that the mass emission coefficient, j_λ, denotes the amount of energy contributing into the direction of consideration. Eq. (3) defines the change in energy in the wavelength interval λ to $\lambda + d\lambda$, due to emission from the elemental mass, dm, into the solid angle $d\omega$ in a time dt. Notice, the solid angle $d\omega$ is the outgoing direction.

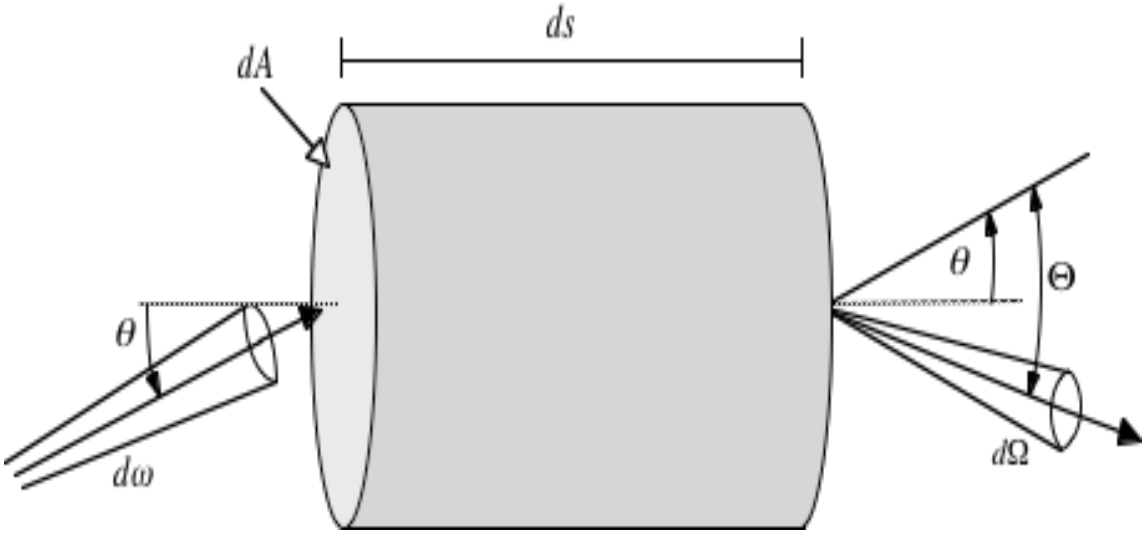

Fig. 2. Traversing Pencil of Radiation. A beam of radiation incident at an angle θ to the volume element is scattered at an angle Θ from the incident direction (adapted from Tynes, 2001).

Consider a scattering and absorbing medium. The increase of energy into the solid angle $d\omega$ is due to the scattering by the medium from all other directions. The radiation propagating from the direction (θ',ϕ') contributes energy into the direction (θ,ϕ) in the amount

$$dE_\lambda = \kappa_{s\lambda} \frac{P(\theta,\phi,\theta',\phi')d\Omega'}{4\pi} I_\lambda(\theta',\phi')dm\, d\lambda\, d\omega\, dt \quad . \tag{4}$$

The (θ',ϕ') and (θ,ϕ) directions are used to determine the scattering angle, Θ. Therefore, the phase function becomes $P(\cos\Theta)$. In radiative transfer problems, the phase function is normalized to one,

$$\frac{1}{4\pi}\int_{4\pi} P(\cos\Theta)d\Omega = \frac{1}{2}\int_0^\pi P(\cos\Theta)\sin\Theta d\Theta = 1 \quad . \tag{5}$$

Upon setting Eq. (4) equal to Eq. (5) and integrating over all incident directions, j_λ is found to be

$$j_\lambda = \frac{\kappa_{s\lambda}}{4\pi} \int_0^{2\pi} \int_0^{\pi} \mathrm{P}(\theta,\phi,\theta',\phi')\, \mathrm{I}_\lambda(\theta',\phi') \sin\theta' \, d\theta' \, d\phi' \,. \tag{6}$$

This is the mass emission coefficient due only to scattering, such that scattering from all directions into the solid angle $d\omega$ of consideration is possible.

Now, examine the energy contribution to the beam due to material emission. Consider a non-scattering medium assumed to be in local thermodynamic equilibrium, i.e. all energy that is absorbed is emitted. The increase of energy into $d\omega$ is due entirely to blackbody emission, defined by the Plank function, $\mathrm{B(T)}$. This term will be left out of the radiative transfer equation, because it is insignificant when considering solar energy at $\lambda \leq 3.5\ \mu m$.[18] Consequently, the change in energy of the incident beam is due solely to absorption and scattering in to and out of the pencil of radiation.

Finally, consider a volume element of thickness ds and cross-section area dA, similar to Fig. 1. The incident energy is perpendicular to dA, ($\cos\theta = 1$), and traverses the distance ds of the volume element to emerge perpendicular to the opposite face with some change in energy. The difference in energy, $d\mathrm{E}$, due to extinction, Eq. (1), and emission, Eq. (4), is

$$d\mathrm{E}_\lambda = -\kappa_{e\lambda}\, \mathrm{I}_\lambda\, \rho\, ds\, d\lambda\, d\sigma\, d\omega\, dt + j_\lambda\, \rho\, ds\, d\lambda\, d\sigma\, d\omega\, dt \,. \tag{7}$$

Emission is due to scattering alone. The total energy difference across ds is proportional to the change in intensity across ds as

$$d\mathrm{E}_\lambda = \frac{d\mathrm{I}_\lambda}{ds}\, ds\, d\lambda\, d\sigma\, d\omega\, dt \,. \tag{8}$$

Finally, the radiative transfer equation takes the very general form

$$\frac{d\mathrm{I}_\lambda}{\kappa_{e\lambda}\rho\, ds} = -\mathrm{I}_\lambda + \mathrm{J}_\lambda \quad , \tag{9}$$

where J_λ is the source function defined as

$$\mathrm{J}_\lambda = \frac{j_\lambda}{\kappa_{e\lambda}} \, . \tag{10}$$

The first term on the right-hand side of the radiative transfer equation (9) is the intensity in the direction (θ,ϕ) due to extinction and the second term is the intensity scattered into the direction (θ,ϕ) from all other directions. At this point, the subscript λ is omitted from the terms in the transfer equation for brevity. However, it is understood that the energy is defined in the wavelength interval λ to $\lambda + d\lambda$.

The radiative transfer equation includes the, direct and diffuse intensity, such that the total intensity, I, is

$$\mathrm{I} = \mathrm{I}_{dir} + \mathrm{I}_{dif} \, . \tag{11}$$

Typically, in radiative transfer problems, the diffuse intensity is sought. In this research, the direct intensity is not considered. The source function is defined by diffuse intensity events and therefore must be kept in the transfer equation. The radiative transfer equation is now defined as

$$\frac{d\mathrm{I}}{\kappa_e \rho ds} = -\mathrm{I} + \mathrm{J} \quad , \tag{12}$$

which includes multiple scattering and only diffuse intensity.

Plane-Parallel Model

An adding-doubling method[23] is used to solve the radiative transfer problem for a plane-parallel atmosphere. The plane-parallel model contains stratified layers, where the only change in the properties of each layer is in the vertical. It is apparent that in the real

atmosphere, especially in observing clouds, this very simplified model may not be completely accurate. However, for our purposes it is an adequate model in which to study the sensitivity of cirrus cloud properties.

In the plane-parallel model, it is quite convenient to consider distances in the vertical. The vertical distance, dz, can be determined from the relationship

$$dz = \cos\theta \, ds \tag{13}.$$

The height, z, is measured upward from the lower boundary of the medium. The angle θ is calculated from the positive z-direction. The azimuth angle, ϕ, is measured clockwise from a plane including the z-axis and another axis, often designated as the x-axis, when looking with the positive z-direction. It is noted that the azimuth angle in this model is represented as the difference in the incident and scattered azimuth angles, $\phi - \phi'$. The direction cosine, $u = -\cos\theta$, and the absolute value, $\mu = |u|$, are defined. The layer is horizontally infinite and vertically finite, with an optical depth of τ'. The plane-parallel system is shown in Fig. 3. Now Eq. (12) depends on z, and is defined according to the geometry of the system as

$$\cos\theta \frac{d\mathrm{I}(z,\theta,\phi)}{\kappa_e \rho dz} = -\mathrm{I}(z,\theta,\phi) + \mathrm{J}(z,\theta,\phi) \tag{14}$$

.

Eq. (14) is further modified, by using $u = -\cos\theta$, so that

$$u \frac{d\mathrm{I}(\tau,u,\phi)}{d\tau} = -\mathrm{I}(\tau,u,\phi) + \mathrm{J}(\tau,u,\phi). \tag{15}$$

The optical thickness of the system is

$$\tau = \int_z^\infty \kappa_e \rho dz. \tag{16}$$

The optical thickness is measured downward from the upper boundary. By Eq. (15), the radiative transfer equation is fully described, including its coordinates, for the plane-parallel model.

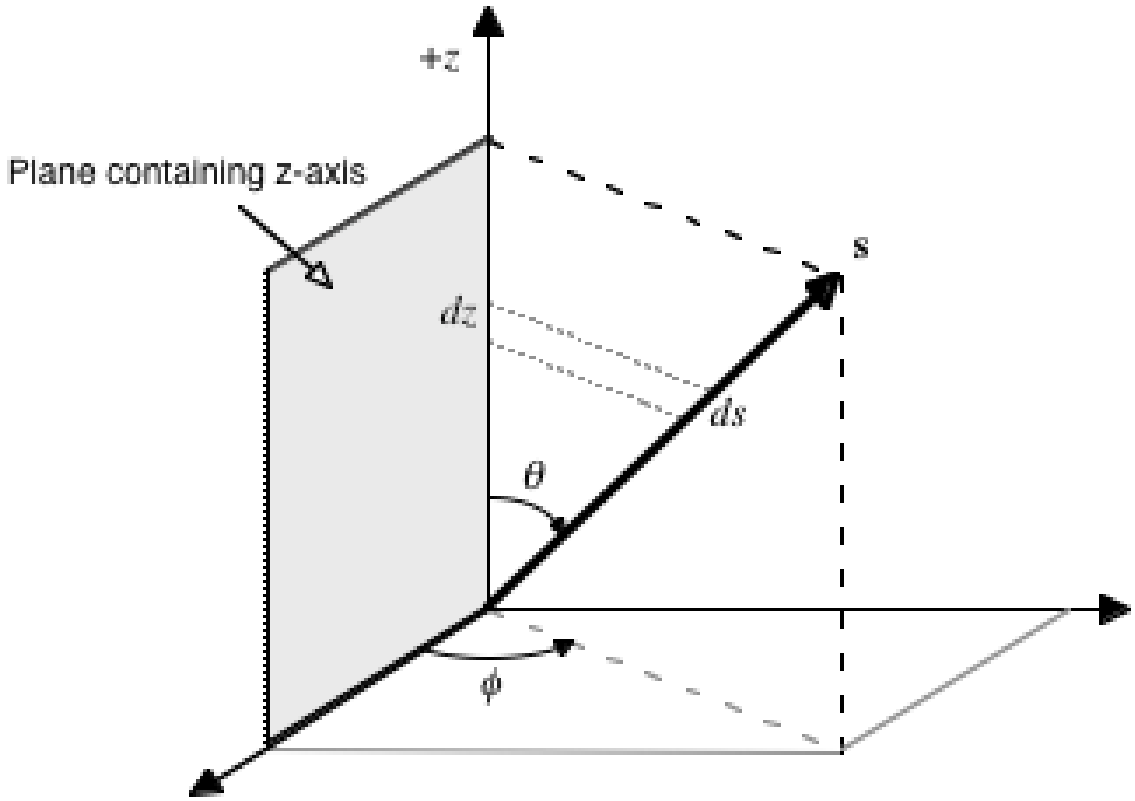

Fig. 3. Plane-Parallel Model. The direction of propagation of the radiation beam is in the s-direction. The component, dz, in the z-direction is determined by considering $\cos\theta$ and the distance ds.

CHAPTER III

POLARIZATION

Vector Form of Radiation

Thus far, the radiative transfer equation has been built in scalar form. To properly define the transfer of radiation in a medium, the vector form of radiation must be included. A vector is defined by its magnitude and direction, and can be described by two components with possibly different complex amplitudes. As shown by Maxwell's equations,[29] light is a transverse wave consisting of electric and magnetic field vibrations perpendicular to the direction of radiation propagation, referred to as electromagnetic radiation. The plane wave solution to Maxwell's equations is essential to the formulation of the vector radiative transfer equation (VRTE). Therefore, to fully explain the nature of electromagnetic radiation, the intensity and the orientation of the radiation must be considered. The orientation of the electromagnetic field as the radiation propagates refers to the polarization state of the radiation field. The terms radiation and light are used interchangeably in place of electromagnetic radiation throughout the text.

Experiments using light initiated the belief that light has orientation. For instance, Malus' experiment[30] revealed that when plane-polarized light was reflected off a galvanized mirror, the orientation of the mirror in reference to the beam of light determined the strength of the reflection. Therefore, the intensity of light varied with respect to the orientation of the mirror. So, the reflection strength depends on the direction of the electric field fluctuations and how they are aligned to the reflection direction due to the mirror orientation. Thus, light must also be defined by its orientation.

Either the electric field component or the magnetic field component can be used to describe light, because one can be determined from the other. Traditionally, the electric field is used and consequently is considered here for the complete description. Any vector can be defined uniquely as a sum of two vectors. The equation describing the planar electric field is

$$\vec{\mathbf{E}} = \vec{\mathbf{E}}_{//} + \vec{\mathbf{E}}_{\perp} = [\mathrm{E}_{//}\hat{\theta} + \mathrm{E}_{\perp}\hat{\phi}]\exp\{-i(\mathrm{k}\hat{n}\cdot\vec{r} - \omega t)\}. \tag{16}$$

The unit vector $\hat{n}$ is the propagation direction of the radiation and is in the meridional plane. The meridional plane is the plane that includes the $+z$-direction and the propagation direction. The vector $\vec{r}$ connects the origin of the local reference frame to the observation point. The unit vectors, $\hat{\theta}$ and $\hat{\phi}$, are perpendicular to the direction of propagation, such that $\hat{n} = \hat{\phi}\times\hat{\theta}$, where $\hat{\theta}$ is in the meridional plane and $\hat{\phi}$ is perpendicular to the meridional plane as shown in Fig. 4. $E_{//}$ and $E_{\perp}$ are the complex amplitudes for each component. The complex amplitudes are defined by the amplitudes, $a_{//}$ and $a_{\perp}$, and the phases, $\delta_{//}$ and $\delta_{\perp}$, of each electric field component. Therefore, Eq. (16) can be written as

$$\vec{\mathbf{E}} = [a_{//}\exp(-i\delta_{//})\hat{\theta} + a_{\perp}\exp(-i\delta_{\perp})\hat{\phi}]\exp\{-i(\mathrm{k}\hat{n}\cdot\vec{r} - \omega t)\}. \tag{17}$$

The complex amplitudes of the electric field are actually space and time dependent. As the radiation propagates, fluctuations in these components consistently occur.[20] The correlation of these two components is discussed in the next section.

Polarization States

As radiation propagates in some direction in time, the magnitude and direction of the electric field varies. In general, this variation can be described by a state of polarization called elliptical polarization. This idea of elliptical polarization is illustrated

in Fig. 5, such that the electric field vector revolves around the propagation axis producing an elliptical pattern as viewed looking into the propagating direction. "Into the propagation direction", means the beam is propagating out of the page.

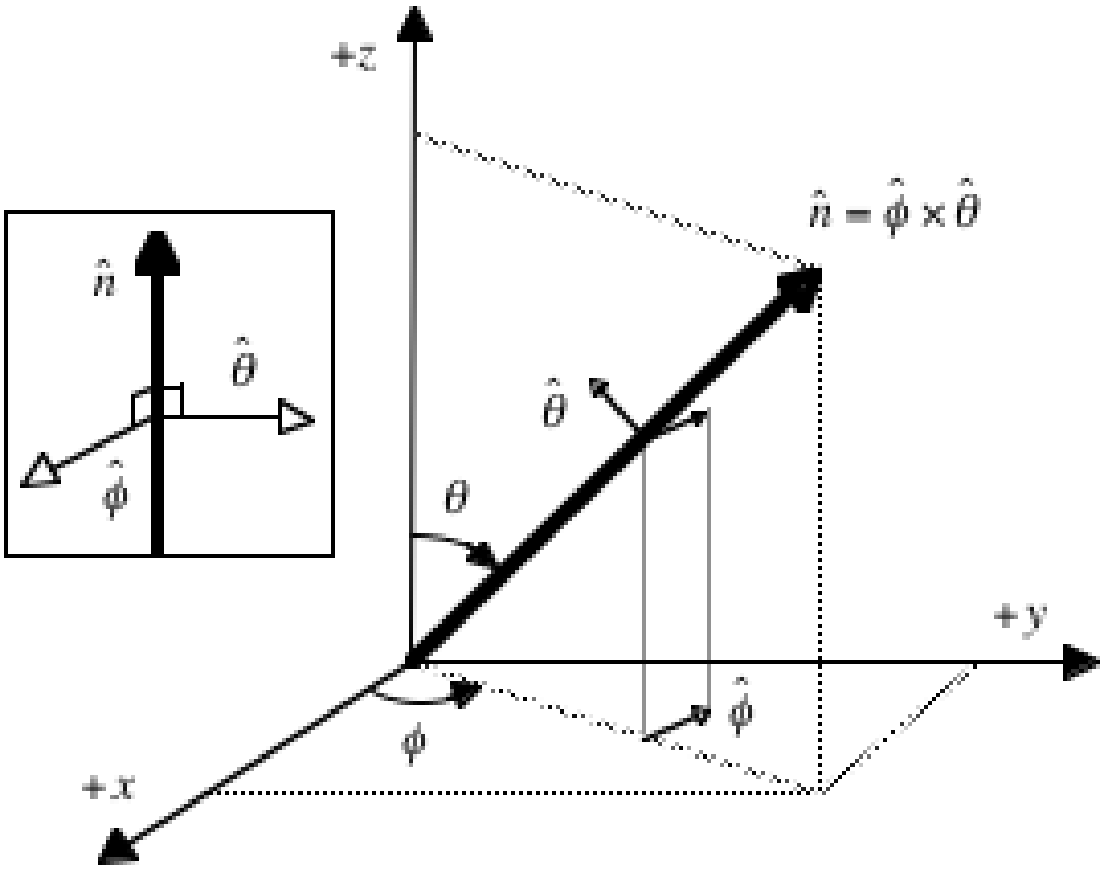

Fig. 4. Electric Field Local Coordinate System. The local coordinate system defines the geometry for describing the propagation direction and orientation of the radiation beam.

The state of polarization of the electric field is described by the amplitudes of the two components and the phase difference, $\delta = \delta_{//} - \delta_{\perp}$, between the two components. The different states of polarization are listed in Table 1.

Table 1. Components of the Polarization States.

Polarization States	Amplitude Components	Phase Difference $\delta = \delta_{//} - \delta_{\perp}$
Elliptical	$a_{//} \neq a_{\perp}$	$\neq 0$ $\neq \pm n2\pi$ $\quad n = 1,\infty$
Linear	$a_{//} \neq a_{\perp}$ or $a_{//} = a_{\perp}$	$= 0$ $= \pm n2\pi$ $\quad n = 1,\infty$
Circular	$a_{//} = a_{\perp}$	$= \pm(2n+1)\frac{\pi}{2}$ $\quad n = 0,\infty$

The electric field components distinguish the polarization states by their amplitudes and phase differences of the electric field components. These values can be entered into Eq. (17), to derive the total electric field.

To have a polarized beam, the variations in the phases and amplitudes must be so that the phase difference, δ, and the ratio of the two amplitudes, $a_{//}/a_{\perp}$, remain constant in time as the radiation propagates.[31] Therefore, the two components are correlated. If the components are uncorrelated as the wave propagates, then there is no preferred state of polarization and the light is unpolarized.

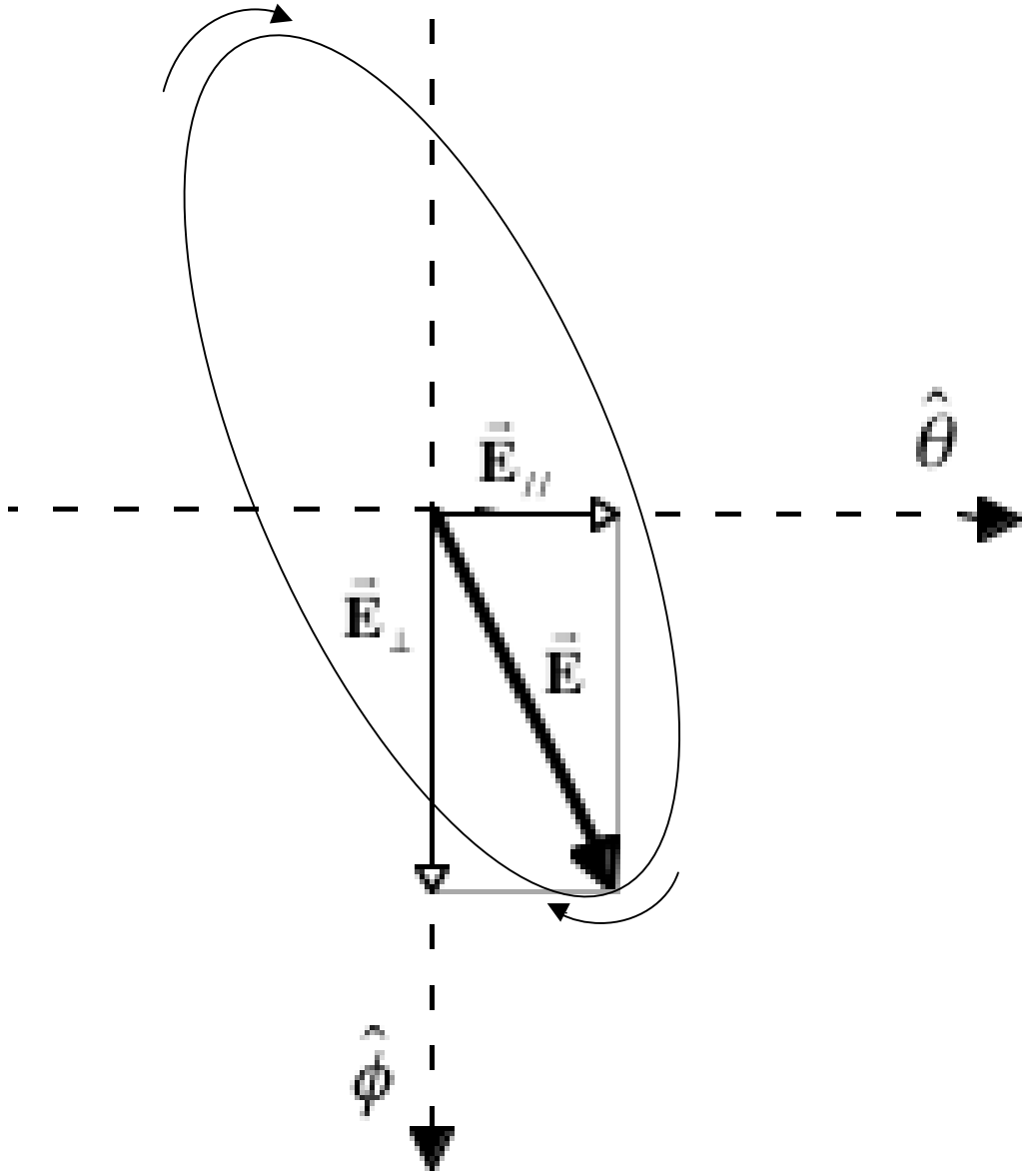

Fig. 5. Elliptical Polarized Beam. The electric field components, $E_{//}$ and $E_{\perp}$, define the electric field vector, $\vec{\mathbf{E}}$. The electric field vector traces out an ellipse in the clockwise direction as the radiation propagates in time (the propagation direction is out of the page).

Light from the sun is considered unpolarized. Birge[32] describes unpolarized light "as a mixture of elliptically polarized components, the ellipses being in every possible shape." Again, unpolarized light has no preference to the state of polarization. The electric field vector traces out an ellipse whose shape varies with time, so that at any given instant the orientation and eccentricity of the ellipse is different than at a previous instant in time. The Stokes parameters provide a simplified way to define polarized and unpolarized light.

Stokes Parameters

A radiation beam can be completely characterized by its intensity and state of polarization. Therefore it would be ideal for us to represent these two characteristics in a form that can be easily introduced into the radiative transfer equation. However, traditional instruments used in light experiments cannot measure the persistent oscillations of the electric and magnetic fields. Instead, these devices measure the time averages of the oscillations in a form that has units of intensity.[20,31] Consequently, representing the polarization state of the radiation beam in the same units is desired.

The set of four parameters introduced by Stokes[24] will be denoted as I, Q, U, and V. These parameters depend on the orientation and amplitude of the electric field vector and are a measurable form of the intensity that includes polarization. They may also be included in radiative transfer problems. The scalar intensity, in the radiative transfer equation, is replaced by the 4×1 vector, of the Stokes parameters, I, Q, U, and V. The Stokes parameters are real values and can be developed from Eq. (16) as

$$\begin{aligned} I &= E_{//}E_{//}^{*} + E_{\perp}E_{\perp}^{*} \\ Q &= E_{//}E_{//}^{*} - E_{\perp}E_{\perp}^{*} \\ U &= E_{//}E_{\perp}^{*} + E_{\perp}E_{//}^{*} \\ V &= i(E_{//}E_{\perp}^{*} - E_{\perp}E_{//}^{*}) \end{aligned} . \tag{18}$$

If the radiation beam is completely polarized, than the relationship

$$I^2 = Q^2 + U^2 + V^2 \tag{19}$$

exists. The Stokes parameters, using the definitions of the complex amplitudes in Eq. (17) and the definition of Stokes parameters in Eq. (18) may be written as

$$\begin{aligned} I &= a_{//}^2 + a_{\perp}^2 \\ Q &= a_{//}^2 - a_{\perp}^2 \\ U &= 2a_{//}a_{\perp}\cos\delta \\ V &= 2a_{//}a_{\perp}\sin\delta \end{aligned} . \tag{20}$$

By using the relationships from Table 1, the different states of polarization are defined by the Stokes parameters. For example, consider the case where the radiation propagates in the $+z$-direction and the intensity of light is unity, so that $I = 1$. If $a_{\perp} = 0$, i.e. no component in the $\hat{\phi}$-direction, then the Stokes vector (I,Q,U,V) takes the form (1,1,0,0). Therefore, the beam is linearly polarized and the vibration of the electric vector is completely in the $\hat{\theta}$-direction.

The polarization state for the ellipse, as traced by the oscillating electric field vector, can also be described by its geometric form. The ellipse is described by its ellipticity and orientation by the angles β and χ in Fig. 6. The Stokes parameters in the geometric form are thus

$$\begin{aligned} \mathrm{I} &= a^2 \\ \mathrm{Q} &= a^2 \cos 2\beta \cos 2\chi \\ \mathrm{U} &= a^2 \cos 2\beta \sin 2\chi \\ \mathrm{V} &= a^2 \sin 2\beta \end{aligned} \quad . \tag{21}$$

The electric field vector that describes this definition of the state of polarization is

$$\vec{\mathbf{E}} = a\hat{p}\cos\beta \sin(\omega t - \mathrm{k}\hat{n}\cdot\vec{r} + \alpha) + a\hat{q}\sin\beta\cos(\omega t - \mathrm{k}\hat{n}\cdot\vec{r} + \alpha), \tag{22}$$

where $\hat{p}$ and $\hat{q}$ are the vectors along the long and short axes of the ellipse, respectively. Eq. (22) is derived from a rotation of the axes from the parallel and perpendicular components, $\hat{\theta}$ and $\hat{\phi}$, of the electric field vector. The intensity is a^2 and α is an arbitrary phase angle. The angle χ describes the orientation of the ellipse measured from the positive $\hat{\theta}$ direction to the $\hat{p}$ direction. The angle is measured in the clockwise direction (radiation propagating out of the page) and has values, $0 \le \chi < \pi$. The angle β describes the ellipticity and ranges from $-\pi/4$ to $\pi/4$.

Polarization states for the geometric representation can also be defined. Consider a beam of unit intensity propagating in the $+z$-direction. If $\beta = 0$, one can easily see that the electric field vector is only oriented in the $\hat{p}$-direction and therefore, is linearly polarized. This corresponds to $\mathrm{Q} = \cos 2\chi$, $\mathrm{U} = \sin 2\chi$, and $\mathrm{V} = 0$. If $\beta = -\pi/4$, then the radiation is left-handed circularly polarized and the Stokes parameters are $(1,0,0,-1)$. Consider the ellipse in Fig. 6, and insert the previous two values of β for the ellipticity angle. It is instantly recognized that linear and circular polarization are special cases of elliptical polarization. For right-handed polarization, β is positive and for left-handed

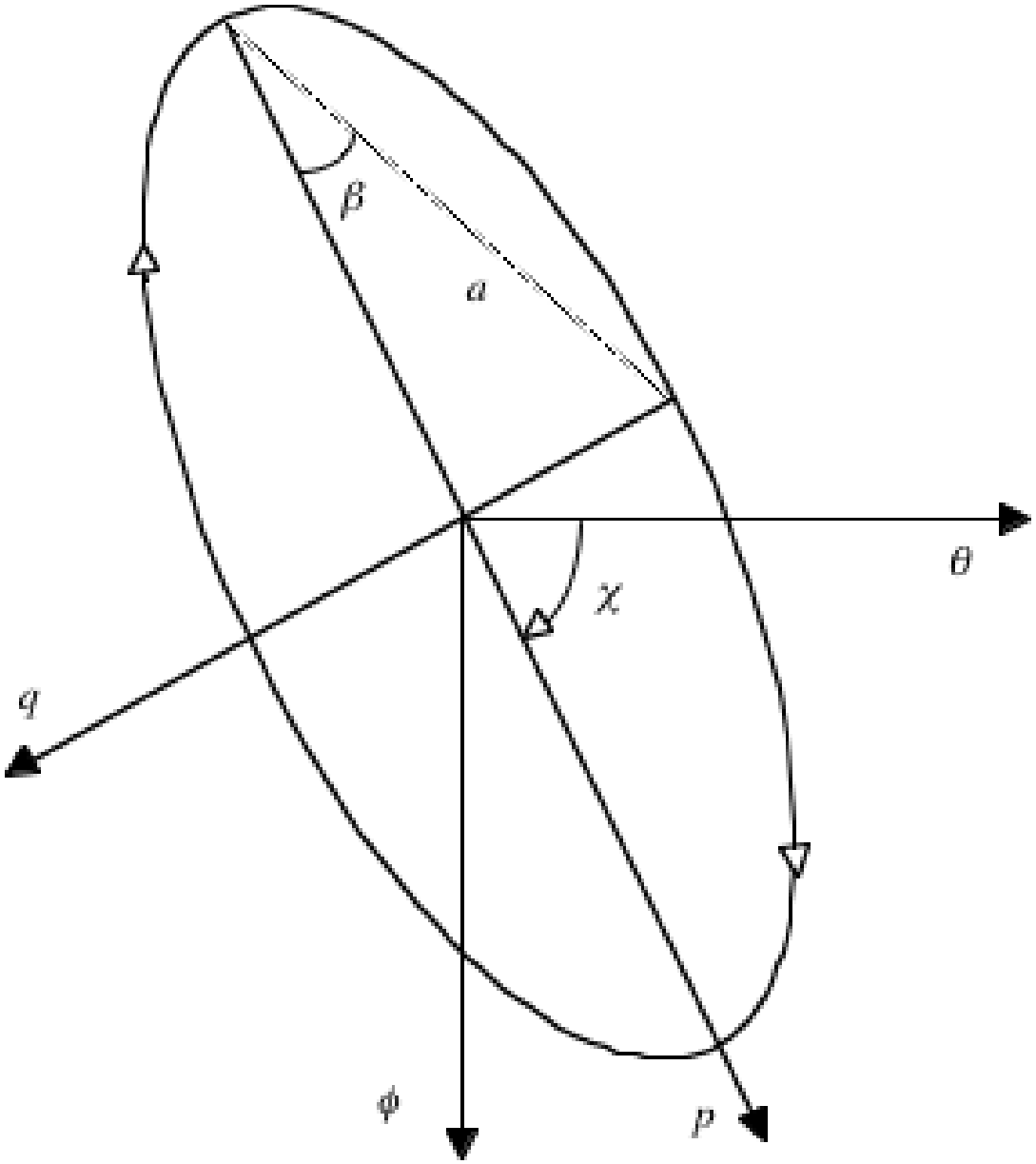

Fig. 6. Geometric Form of the Ellipse. The electric field vector rotates around the propagation axis in the clockwise direction. This is known as left-handed elliptically polarized radiation. The propagation direction is out of the page. For this case $\beta < 0$.

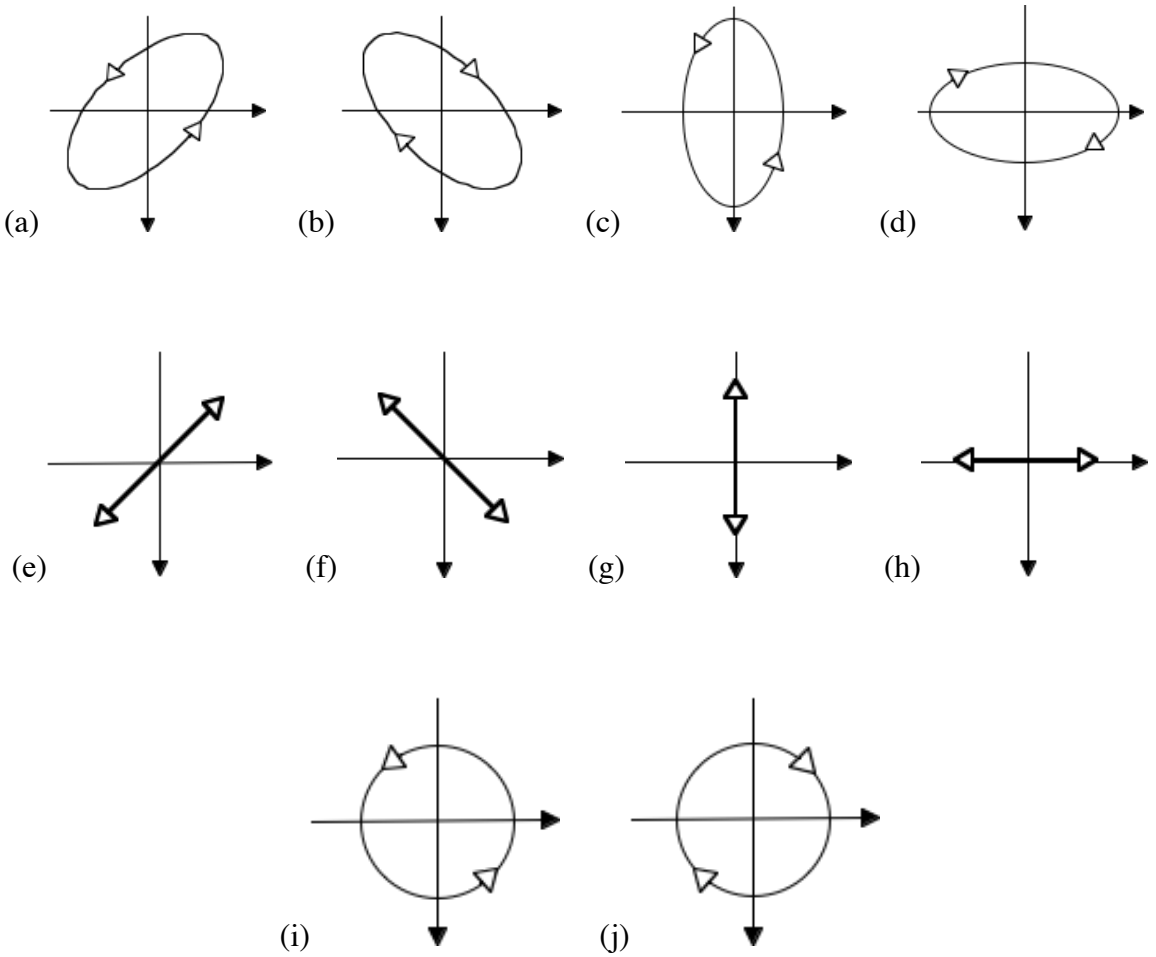

Fig. 7. Polarization States Using Stokes Parameters. The top row and bottom row are elliptical and circular polarization, respectively, of different orientations and handedness. The middle row is linear polarization of different orientations. For graphs (a) and (e), $\chi = 3\pi/4$ and for graphs (b) and (f), $\chi = \pi/4$. The Stokes parameters for each figure are: (a) $Q = 0 \;\; U < 0 \;\; V > 0$, (b) $Q = 0 \;\; U > 0 \;\; V < 0$, (c) $Q < 0 \;\; U = 0 \;\; V > 0$, (d) $Q > 0 \;\; U = 0 \;\; V < 0$, (e) $Q = V = 0 \;\; U = -I$, (f) $Q = V = 0 \;\; U = I$, (g) $U = V = 0 \;\; Q = -I$, (h) $U = V = 0 \;\; Q = I$, (i) $Q = U = 0 \;\; V = I$, (j) $Q = U = 0 \;\; V = -I$.

polarization β is negative, as viewed looking into the beam. Therefore, the electric field vector rotates counter-clockwise for right-handed polarization and clockwise for left-handed polarization. One must be careful when using Stokes parameters, particularly for the definition of handedness. Figure 7 presents more cases of the different states of polarization. Figure 7 is similar to the figures presented by Mishchenko and Travis;[31] however, their definitions of the Stokes parameters are different.

So far, the amplitudes and phases of the components are assumed to have no time dependence. In actuality, small fluctuations occur in the complex amplitudes of the electric field and vary slower than the period of vibration, but frequent enough to be undetectable by measurement. Therefore, optical instruments are unable to detect the instantaneous Stokes parameters, but instead detect a time average of millions of simple waves of independent phases. The time average is denoted with brackets as described by Hansen and Travis.[33] Now, because of these fluctuations, Eq. (19) becomes

$$I^2 \geq Q^2 + U^2 + V^2. \tag{23}$$

Therefore, light is generally partially polarized, where the beam is a mixture of polarized and unpolarized light. The equality only holds if the components of the electric field are correlated, i.e., completely polarized.

The Stokes vector for unpolarized light makes more sense when considering the average. As mentioned in the Polarization States section, there is no dominant state of polarization. So, the complex amplitudes vary with time and are not correlated. Therefore, the phases of the components are not related, and the time averages of $\cos\delta$ and $\sin\delta$ from Eq. (20) equal zero. Also, the average amplitudes of the two components

in time are equivalent, $\langle a_{//} \rangle = \langle a_{\perp} \rangle$. The Stokes vector for a beam of unpolarized light is thus $(1,0,0,0,)$.

The Stokes parameters by the principle of optical equivalence[34] are the complete set of quantities necessary to characterize the intensity and state of polarization of light. Consequently, any two beams with the same Stokes parameters are equivalent. Their intensity and state of polarization are the same, despite possible differences in the phases of their components, which are experimentally indistinguishable. Even if two beams are produced by two different media, optical analysis is unable to further differentiate these beams.

Finally, what makes Stokes parameters so desirable is the ability to add them together when considering incoherent beams of light. If each beam is independent of another beam in the same direction, so that their phases are independent, Stokes parameters are additive. Their application is quite useful in experimental work where the incident Stokes parameters are altered by the interaction with the optical medium to produce the outgoing or scattered Stokes parameters. This relationship, is of the form

$$\mathbf{I} = \begin{bmatrix} I_s \\ Q_s \\ U_s \\ V_s \end{bmatrix} = \mathbf{M} \begin{bmatrix} I_0 \\ Q_0 \\ U_0 \\ V_0 \end{bmatrix}. \tag{24}$$

The Mueller matrix, $\mathbf{M}$, is a 4×4 matrix that completely describes the optical instrument or some physical process, such as scattering[35] by its optical properties, and transforms the incident Stokes parameters into the scattered Stokes parameters.[34] The Mueller matrix is determined in this research to possibly gain information about the medium of transfer.

Mueller Matrix

Again, the Mueller matrix completely describes the system one is considering. Therefore, if the Mueller matrix is known for the cirrus cloud layer, than all the information that describes the cirrus cloud is known because it is found in the Mueller matrix. Consequently, information about the constituents, the microphysical properties, and the optical properties are available. The Mueller matrix provides 15 more elements of information than are available by just considering the scalar intensity of the scattered beam. For these reasons and to encourage future work in remote sensing, the Mueller matrix is described and studied as a method to help distinguish cirrus cloud properties.

In experimental work,[36] the elements of the Mueller matrix for a medium can be calculated by considering 49 different vector intensity measurements. In this research, the Mueller matrix is determined by illuminating the ice crystal layer with only four different incident states of polarization. The four incident states of polarization are: linearly polarized $(1,1,0,0)$, linearly polarized at $\chi = 45^\circ$ $(1,0,1,0)$, right-circularly polarized $(1,0,0,1)$ and unpolarized $(1,0,0,0)$ radiation. The Mueller matrix is

$$\mathbf{M}(\mu,\mu',\phi-\phi') = \begin{bmatrix} \mathrm{M}_{11} & \mathrm{M}_{12} & \mathrm{M}_{13} & \mathrm{M}_{14} \\ \mathrm{M}_{21} & \mathrm{M}_{22} & \mathrm{M}_{23} & \mathrm{M}_{24} \\ \mathrm{M}_{31} & \mathrm{M}_{32} & \mathrm{M}_{33} & \mathrm{M}_{34} \\ \mathrm{M}_{41} & \mathrm{M}_{42} & \mathrm{M}_{43} & \mathrm{M}_{44} \end{bmatrix}, \tag{25}$$

where each element is determined by rearranging Eq. (24) as

$$\mathbf{M}(\mu,\mu',\phi-\phi') = \frac{\mathrm{I}_s}{\mathrm{I}_0}, \tag{26}$$

and applying each incident polarization state. The Mueller matrix is dependent on the geometry of the system. It also depends on the properties of the system, which is evident in the next section.

Vector Radiative Transfer Equation

To describe the scattering process of any medium, consider a sample of the constituents of that medium, represented by some size distribution. Now, the scattering process of the sample is described by a 4×4 matrix, $\mathbf{P}(\Theta)$, known as the average scattering matrix. The scattering matrix is defined in the scattering plane, which contains the incident beam and scattered beam. Since, the Stokes parameters are defined in the meridian plane of the system, which includes the direction of propagation and the $+z$-direction, the necessary rotations must be performed on the scattering matrix. The phase matrix is defined as

$$\mathbf{Z}(\theta,\phi;\theta',\phi') = \mathbf{L}(\pi - \sigma_2)\mathbf{P}(\Theta)\mathbf{L}(-\sigma_1), \tag{27}$$

where the incident meridian plane is rotated into the scattering plane at the angle σ_1 and then rotated into the scattered meridian plane at the angle σ_2. The rotation matrix takes the general form

$$\mathbf{L}(\sigma) = \begin{bmatrix} 1 & 0 & 0 & 0 \\ 0 & \cos 2\sigma & \sin 2\sigma & 0 \\ 0 & -\sin 2\sigma & \cos 2\sigma & 0 \\ 0 & 0 & 0 & 1 \end{bmatrix}, \tag{28}$$

The rotation angles and the scattering angle are determined using the geometry of the scattering system.[37]

Now, the radiative transfer equation defined in Eq. (15), can be written in vector form as

$$u\frac{d\mathbf{I}(\tau,u,\phi)}{d\tau} = -\mathbf{I}(\tau,u,\phi) + \mathbf{J}(\tau,u,\phi), \tag{29}$$

which now includes polarization. The source function becomes

$$\mathbf{J}(\tau,\mu,\phi) = \frac{\varpi}{4\pi}\int_0^{2\pi}\int_{-1}^{1}\mathbf{Z}(u,u',\phi-\phi')\mathbf{I}(\tau,u',\phi')du'\,d\phi', \tag{30}$$

where the phase matrix is dependent on u, u', and $\phi-\phi'$ and the single-scattering albedo, ϖ, is introduced. The single-scattering albedo is the fraction of scattered energy to the total amount of energy removed from the incident beam. Eq. (29) describes the change in the radiation due to a medium and now includes polarization. It is known as the vector radiative transfer equation (VRTE).

Adams and Kattawar[38] show that, in a medium where Rayleigh scattering occurs, there are significant differences between the scalar intensity, without polarization, and vector intensity, including polarization. Lenoble[26] documents errors of up to 10% for Rayleigh scattering. Hansen[39] discusses more radiative transfer models and shows errors in intensities up to 1% for spherical droplets of sizes on order of or larger than the wavelength, via an adding-doubling method. It is believed that similar errors occur for non-spherical particles. Although, the errors are small for larger particles, the state of polarization of the scattered light yields information about the medium of transfer. Therefore, the radiative transfer equation shall be formulated to include polarization.

CHAPTER IV

CIRRUS CLOUDS AS A MEDIUM FOR TRANSFER

Before the VRTE is solved, the single-scattering properties must be derived. First, the light scattering properties of a small volume of randomly oriented ice crystals will be calculated. Second, bulk and average scattering properties for a collection of particles are determined. Third, the average scattering properties are applied to the VRTE to calculate the total reflected radiation field of the medium. First, certain assumptions must be considered in calculating the single-scattering properties for an ice crystal.

Geometrical Optics

In light scattering with an ice crystal, assumptions can be made about the light interaction with that ice crystal. If the particle is much larger than the wavelength of light, than the geometrical optics approach may be used to approximately compute the angular distribution of scattered light. This approach assumes that light can be separated into localized rays parallel to the propagation direction. Geometric optics provides asymptotic approximations of the fundamental electromagnetic theory for light scattering,[18] such that the results are more accurate as the size to wavelength ratio goes to infinity.

Consider a plane wave incident on some arbitrary particle (Fig. 8). The plane wave is divided into many small increments along the wave front and the propagation of the wave is normal to the wave front. Each increment of the plane wave, if considered a ray, is allowed to pursue its own rectilinear path through the particle as determined by Snell's law. The wave front of a plane wave can be visualized as many points that act as a source of wavelets. These wavelets propagate forward in spherical waves and produce a new wave front at the envelope of the wavelets, where the phase is constant. This is

known as Huygens' principle. This definition of the plane wave is convenient when considering reflection and refraction due to an interface separating different media.

The geometric optics approach requires the size of the obstructing particle to be much larger than the wavelength of the incident light. Also, the width of the increment for each ray must be larger than the wavelength, but smaller than the particle. This assumption allows one to consider the plane wave solution to describe each ray. There are four geometrical optics laws: rectilinear propagation, reflection, refraction, and reversibility. Rectilinear propagation assumes that light always proceeds in a straight line. Therefore, diffraction is neglected. Huygens' principle helps to explain the laws of reflection and refraction: at each point on the surface of the particle where reflection and refraction occur, source wavelets are initiated. The propagation of the these wavelets create a wave front in a different direction from the incident beam depending on the angle of incidence and the index of refraction. Finally, the reversibility law requires that if the incident direction is reversed than the light will follow the same path it traveled before it was reversed but in the opposite direction. Although, diffraction is not a part of geometric optics, it definitely must be incorporated.

Diffraction is important because it occurs in any experiment using light. We will consider two parts to diffraction in a scattering process. First, consider the assumption that the width of the ray must be larger than the wavelength. If the width of the ray is too small, the individual rays cannot be approximated as a plane wave and the diffraction due to the phase interferences across the wave is quite strong. Basically, if there is any limitation to the width of the beam, there will be diffraction.[30] Second, the light that passes near a particle is diffracted, such that the energy is removed from that

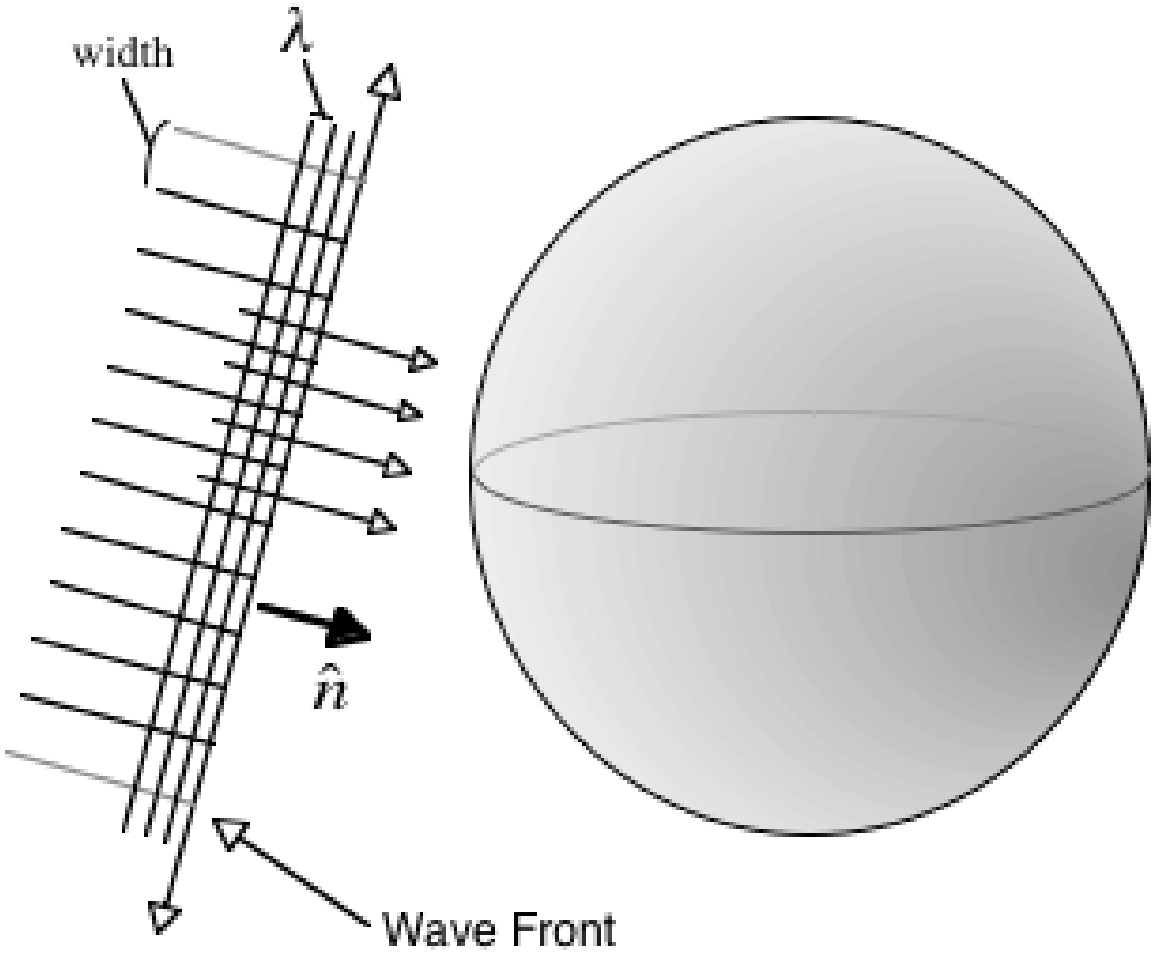

Fig. 8. Plane Wave Incident on a Particle. The propagation direction of the plane wave is denoted by $\hat{n}$. The plane wave is divided into many rays propagating in the same direction as $\hat{n}$. The wavelength, λ, is much smaller than the width of the rays. As each ray interacts with the particle, it is allowed to pursue its own path, reflected away from or refracted through the particle.

light wave. Diffraction becomes more significant as the particle size to wavelength ratio gets larger. The presence of the particle bends the light passing close to the particle so that it is concentrated in a narrow lobe in the forward direction. It is this diffraction that creates the scattered energy maximum in the forward direction, portrayed by the phase function of an ice crystal (Fig. 9).

To calculate the complete scattering field due to an ice crystal, other aspects of light interaction must be included. First, it is noted that even for large widths, interactions of the wavelets cause phase interferences. Yang and Liou[40] describe this divergence of the energy from the forward direction. Second, the polarization state of the ray must be acknowledged because any interaction with the ice crystal interface can induce a change in polarization. Finally, larger ice crystals create significant diffraction such that rectilinear propagation breaks down, and light is bent around the outside of the crystal.

According to Yang and Liou,[17] their geometric optics model allows accurate calculation of the phase functions and scattering efficiencies for size parameters as small as 20. Yang and Liou[40] extended their method to calculate the scattering matrix, extinction efficiency and single-scattering albedo for the 3-D case. The above geometric optics method by Yang and Liou[17,40] and the combined ray-by-ray algorithm[41] are known as the Improved Geometric Optics Method (IGOM). IGOM combines geometric optics, diffraction, and polarization to calculate the single-scattering properties for ice crystals. IGOM is used in this research to calculate those properties for various ice crystal sizes and habits.

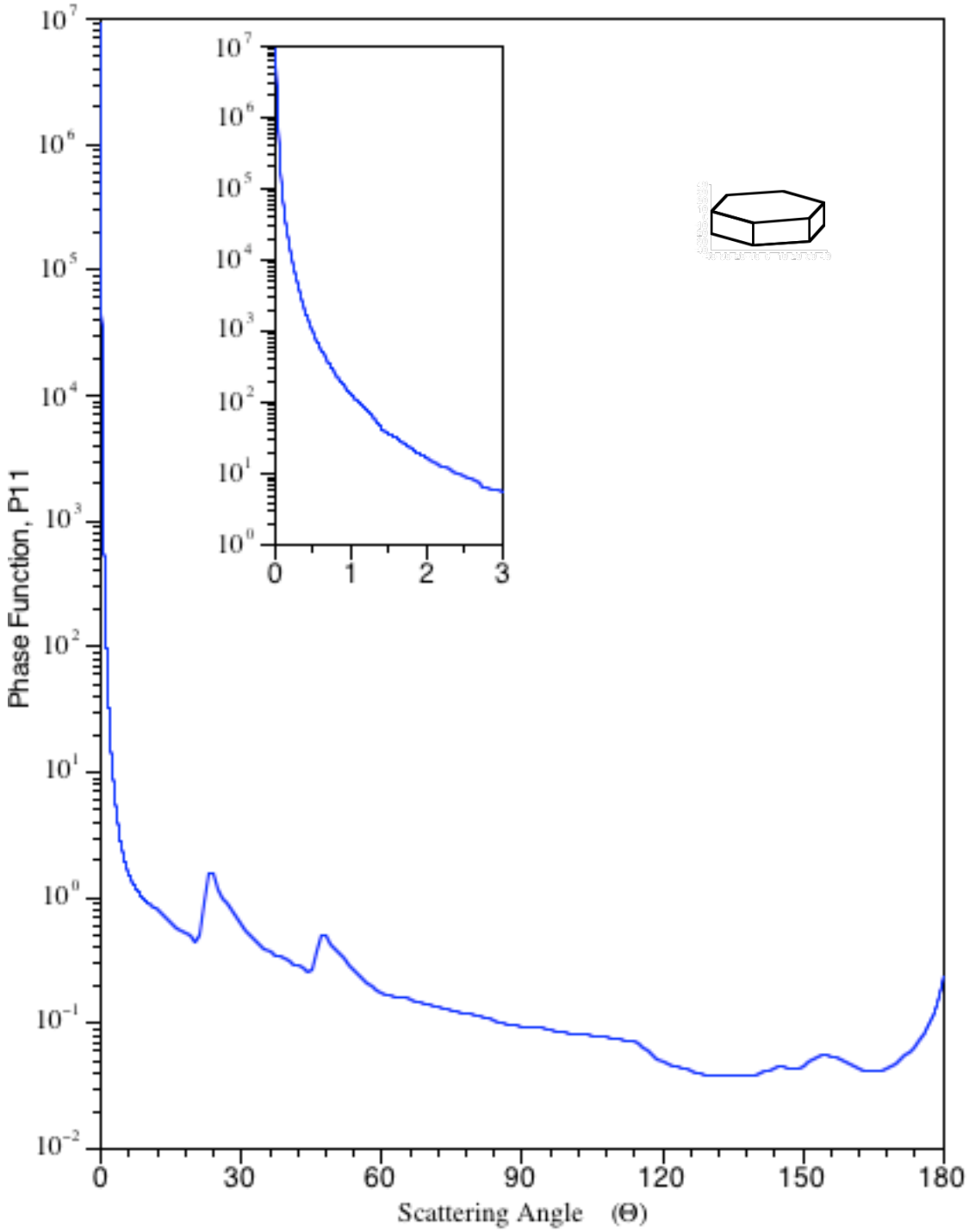

Fig. 9. Phase Function Including Forward Peak. The phase function of plate is displayed determined by IGOM for $\lambda = 0.532\ \mu m$ and $D_e = 100.25\ \mu$m. The diffraction peak in the forward direction is of magnitude seven times stronger than the backscattering direction.

Average Single-Scattering Properties

If the medium is a cirrus cloud than the single-scattering properties are determined by considering the ice crystals that make up the cloud. Given a wavelength of light and the polarization of the incident beam, as well as, the size, shape, and the orientation of an ice crystal, and with a formulating idea of scattering through that ice crystal, the single-scattering properties can be obtained. The properties necessary as input into the radiative transfer model are the optical depth, single-scattering albedo and scattering matrix. The albedo and scattering matrix are determined using IGOM.

Generally, light that is scattered is polarized. The following equations, therefore, describe the scattered electric field including polarization. van de Hulst[34] describes, very well, the transformation from an incident light wave with respect to some reference plane to a scattered light wave with respect to another reference plane by the transformation matrix, $\mathbf{S}$, which is made of four complex amplitude functions dependent on the incident and outgoing directions. The complex amplitude functions are

$$\mathbf{S} = \begin{bmatrix} S_2 & S_3 \\ S_4 & S_1 \end{bmatrix}. \tag{31}$$

These functions describe the amplitude and phase of the scattered wave and hence its polarization.

The general equation for the electric field is described by Eq. (16) in Section III. Most observations of the scattered field are obtained in the far field, where $kr >> 1$.[18] With reference to the definition of the electric field vector in Eq. (16) and Eq. (31), the scattered wave in the far field becomes

$$\begin{bmatrix} E^s_{//} \\ E^s_{\perp} \end{bmatrix} = \frac{\exp(-ikr + ik\eta)}{ikr} \begin{bmatrix} S_2 & S_3 \\ S_4 & S_1 \end{bmatrix} \begin{bmatrix} E^i_{//} \\ E^i_{\perp} \end{bmatrix}. \tag{32}$$

The transformation matrix depends on the directions of incidence and scattering and the orientation the ice crystal. The term η is an arbitrary propagation direction of the incident beam and is often denoted in the literature[18,34] as z, being in the $+z$-direction.

The scattered Stokes parameters are calculated using Eq. (32) and the definition of the Stokes parameters in Eq. (18). The scattered Stokes parameters for light incident on a single ice crystal becomes

$$\begin{bmatrix} I_s \\ Q_s \\ U_s \\ V_s \end{bmatrix} = \frac{\sigma_s \mathbf{P}}{4\pi r^2} \begin{bmatrix} I_0 \\ Q_0 \\ U_0 \\ V_0 \end{bmatrix}. \tag{33}$$

The single-scattering matrix, **P**, describes the angular distribution of light scattered by the ice crystal and is derived directly from the complex amplitude functions. Notice the similarities to the Mueller matrix first defined in Eq. (24). The scattering matrix and the Mueller matrix are proportional for the case of single-scattering. The scattering cross section, σ_s, is the amount of energy that is removed from the incident beam due to scattering and figuratively represents an isotropic redistribution of that energy on the surface of a sphere with some radius from the center of an ice crystal.[18] The scattering cross section is the integration over all scattering angles of the first element of the scattering matrix:

$$\sigma_s = \frac{1}{k^2} \int_0^{2\pi} \int_0^{\pi} (E_{//}^s E_{//}^{s*} + E_{\perp}^s E_{\perp}^{s*}) \sin\theta \, d\theta \, d\phi \,. \tag{34}$$

The basic setup of the scattering matrix is

$$\mathbf{P}(\Theta,\alpha,\gamma) = \begin{bmatrix} P_{11} & P_{12} & P_{13} & P_{14} \\ P_{21} & P_{22} & P_{23} & P_{24} \\ P_{31} & P_{32} & P_{33} & P_{34} \\ P_{41} & P_{42} & P_{43} & P_{44} \end{bmatrix}, \tag{35}$$

where it depends on the scattering angle Θ and on the ice crystal orientation with respect to the incident beam. To simplify Eq. (35), consider a small sample volume, of randomly oriented particles of all the same size. The scattering matrix of this sample is obtained by integrating over all orientations for each ice crystal:

$$\mathbf{P}(\Theta) = \frac{1}{2\pi\sigma_s}\int_0^{2\pi}\int_0^{\pi/2}\mathbf{P}(\Theta,\alpha,\gamma)\sigma_s(\alpha,\gamma)\sin\alpha\, d\alpha\, d\gamma \,. \tag{36}$$

This form of the scattering matrix is no longer dependent on the direction of the incident wave. Similarly, the scattering cross section is found to be

$$\sigma_s = \frac{1}{2\pi}\int_0^{2\pi}\int_0^{\pi}\sigma_s(\alpha,\gamma)\sin\alpha\, d\alpha\, d\gamma \,. \tag{37}$$

Further simplifications of the scattering matrix are obtained by assuming symmetry relationships exist. van de Hulst[34] describes three orientations of a particle that can be related to some initial position, in which two orientations have a mirror particle. If we further assume that a sample of randomly oriented ice crystals have an equal number of their mirror images, Eq. (35) simplifies to

$$\mathbf{P}(\Theta) = \begin{bmatrix} P_{11} & P_{12} & 0 & 0 \\ P_{12} & P_{22} & 0 & 0 \\ 0 & 0 & P_{33} & -P_{43} \\ 0 & 0 & P_{43} & P_{44} \end{bmatrix}. \tag{38}$$

Now, there are only six independent elements in the scattering matrix. The first element, P_{11}, the phase function is normalized by Eq. (5). The other elements of the scattering matrix are normalized, for instance as

$$\left|\frac{P_{12}}{P_{11}}\right| \le 1 \quad . \tag{39}$$

Now, the scattering properties for a population of ice crystals may be sought.

To calculate the average and bulk scattering properties, representative size distributions and habit distributions of cirrus clouds are needed. The single-scattering properties of individual ice crystals are averaged together using size distributions and habit distributions for different sizes and shapes. The bulk scattering properties are used to define a spatial volume that describes cirrus clouds in a GCM grid box.[10] Therefore, an average over size and habits must be taken.

An average size for each size distribution is defined by the effective size, D_e, where the volume, V, projected area, A, and size distribution, n, depend on the ice crystal maximum dimension, L. The effective size as defined by Yang et al.[42] and used in this study is

$$D_e = \frac{3}{2}\frac{\int_{L_{\min}}^{L_{\max}} V(L)n(L)dL}{\int_{L_{\min}}^{L_{\max}} A(L)n(L)dL} \quad . \tag{40}$$

Also, the mean extinction and absorption efficiency are defined as

$$Q_{e,a} = \frac{\int_{L_{\min}}^{L_{\max}} Q_{e,a}(L)A(L)n(L)dL}{\int_{L_{\min}}^{L_{\max}} A(L)n(L)dL} \quad , \tag{41}$$

where e and a indicate the extinction and absorption efficiency, respectively. Q_e is defined as the extinction cross section divided by the projected area of the particle. The single-scattering albedo is related to the extinction and scattering efficiency as

$$\varpi = 1 - \frac{Q_a}{Q_e} \quad . \tag{42}$$

Notice, if $Q_a = 0$, then $\varpi = 1$ and all extinction of the incident beam is due to scattering.

The average scattering matrix is determined using the following equation:

$$\mathbf{P}(\Theta) = \frac{\int_{L_{\min}}^{L_{\max}} \mathbf{P}(\Theta, L)(Q_e(L) - Q_a(L))A(L)(L)n(L)dL}{\int_{L_{\min}}^{L_{\max}} (Q_e(L) - Q_a(L))A(L)n(L)dL} . \qquad (43)$$

$\mathbf{P}(\Theta, L)$ is the scattering matrix calculated in Eq. (36) for each size ice crystal.

Now, that the scattering properties and scattering model are defined, consider the initial input into the model and the results that were obtained. The single-scattering properties for 38 size bins at $\lambda = 0.532 \mu m$ for four habits, aggregate, bullet rosette, plate and hollow column were determined. The average properties were then computed using the size distributions mentioned in Section II. The mixed habit percentages used by Baum et al. are display in Table 2. These percentages are for the middle latitudes taken from data collected during the FIRE campaigns. L_{avg} is the average length of the ice crystal for each size bin, where the minimum length and the maximum length are averaged together.

Table 2. Mid-Latitude Habit Percentages for a Mixed Habit Cirrus Cloud.

Habits	$L_{avg} < 70 \mu m$	$L_{avg} > 70 \mu m$
Bullet Rosette	50%	30%
Aggregate	0%	30%
Plate	25%	20%
Hollow Column	25%	20%

CHAPTER V

THE ADDING-DOUBLING METHOD

The equations for the adding-doubling method, including multiple scattering, were presented by van de Hulst.[22] In the second paper by Takano and Liou,[19] the transfer of radiation including polarization in an anisotropic medium of randomly oriented and oriented ice crystals is computed for incident solar radiation by an adding method. In the next couple of chapters, the reflected vector intensities are calculated for various optical depths, incident solar angles, viewing angles, and different ice crystal habits and effective sizes, using an adding-doubling method by Haan et al.[23]

Concept

Consider a plane-parallel layer, slab 1, with optical thickness τ_1 and another layer, slab 2, of optical thickness τ_2, immediately below slab 1 in the atmosphere. If the reflection and transmission matrices for slab 1, $(\mathbf{R}_1,\mathbf{T}_1)$, and for slab 2, $(\mathbf{R}_2,\mathbf{T}_2)$, are known, then the reflection and transmission matrices, $(\mathbf{R}_c,\mathbf{T}_c)$, for the combined layer can be determined (Fig. 10) by a system of adding equations. The combined layer has optical depth, $\tau_1 + \tau_2$. From these matrices the intensity throughout the layer may be determined. The matrices of the combined layer include the infinite number of reflections occurring between slab 1 and slab 1, therefore incorporating multiple scattering.

These two layers may be vertically inhomogeneous of different composition and optical depth. If the matrices are not known, then each layer is divided into many smaller optically thin layers so to approximate one or two orders of scattering and to obtain a homogeneous layer. Now the reflection and transmission matrices are determined for the

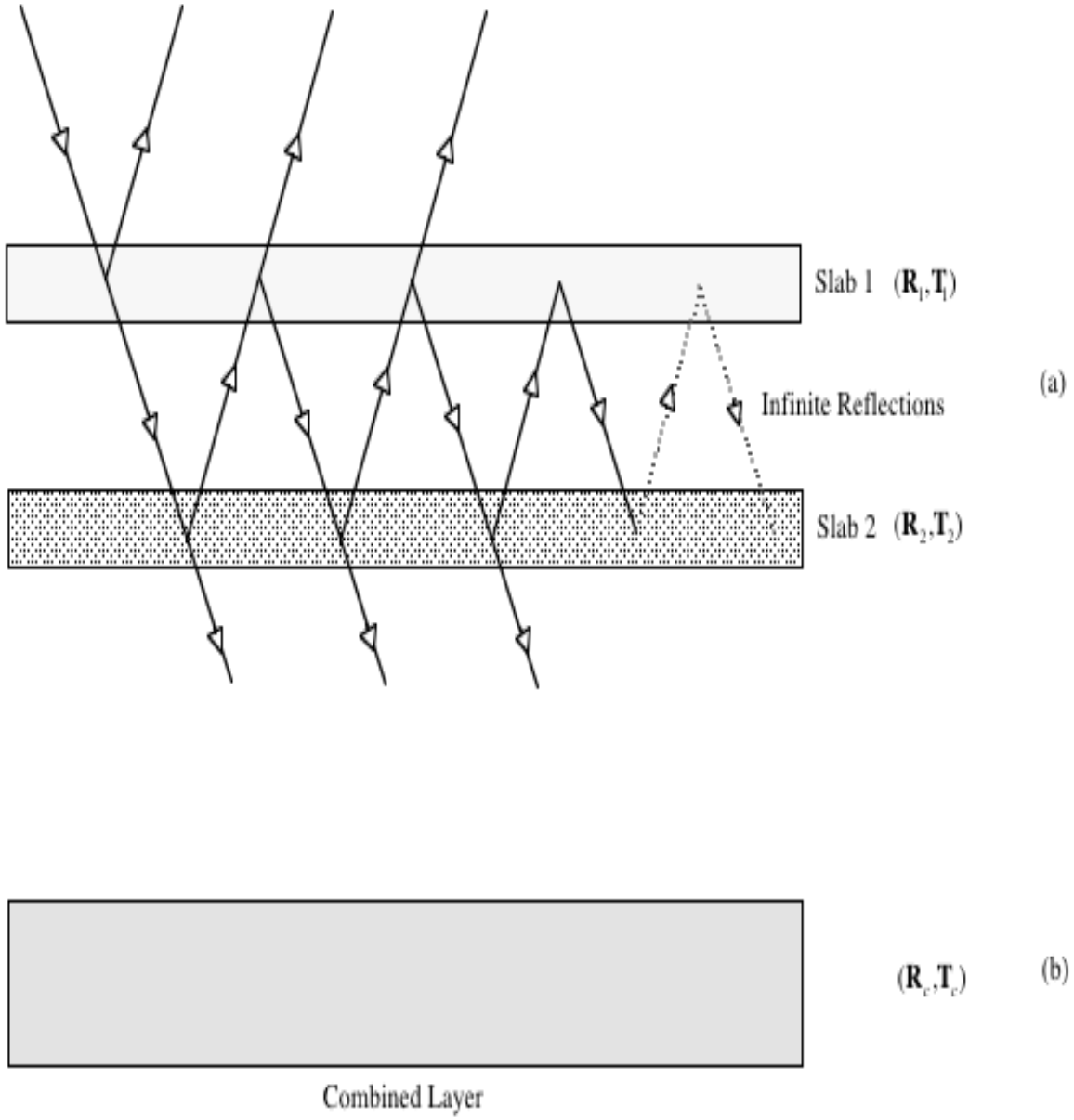

Fig. 10. Basic Adding of Two Layers. Radiation is incident on the top of layer 1 and then proceeds to reflect from and transmit through both layers 1 and 2. (a) The reflection and transmission matrices define the properties for each layer. (b) The reflection and transmission matrices for the combined layer are determined from those of the two layers, 1 and 2.

optically thin homogeneous layer. The matrices are applied to the adding equations to find those matrices for a combined layer. After adding many layers, eventually the matrices for the entire layer are calculated.

Another approach to determine the properties of the entire layer is the doubling method. If the two layers are identically homogeneous, then the doubling method is applied. Consider, the reflection and transmission matrices for the optically thin layers, determined before, but the optical depth of each layer is the same. If many homogeneous layers are calculated then the doubling method is faster than the adding method, because repeated calculations of the initial reflection and transmission matrices for each layer is not necessary. The process of doubling the optical thickness is performed until the optical thickness of the initial layer, before the layer is divided, is met.

In this research, there is no dependence of the scattering properties of the medium on the optical thickness. Therefore, each thin layer is identical and homogenous. Therefore, the doubling method is used to compute the scattering properties of the entire cirrus cloud layer.

The Adding Equations

Before submitting the adding equations, it must be understood what is desired from these equations. To explain the propagation of radiation upwards and downwards at any depth in the atmosphere, two matrices, $\mathbf{U}(\tau,\mu,\mu',\phi-\phi')$ and $\mathbf{D}(\tau,\mu,\mu',\phi-\phi')$ are considered. These matrices are defined by the equations

$$\mathbf{I}(\tau,\mu,\phi)=\frac{1}{\pi}\int_0^{2\pi}\int_0^1\mathbf{D}(\tau,\mu,\mu',\phi-\phi')\mathbf{I}(0,\mu',\phi')\mu'\,d\mu'\,d\phi' + \exp[-\tau/\mu]\,\mathbf{I}(0,\mu,\phi) \tag{44}$$

and

$$\mathbf{I}(\tau,-\mu,\phi) = \frac{1}{\pi}\int_0^{2\pi}\int_0^1 \mathbf{U}(\tau,\mu,\mu',\phi-\phi')\mathbf{I}(0,\mu',\phi')\mu' d\mu' d\phi' , \tag{45}$$

where $\mathbf{I}(0,\mu',\phi')$ is the intensity incident at the top of the layer. The equations give the intensity of radiation traveling downwards, $\mathbf{I}(\tau,\mu,\phi)$, and upwards, $\mathbf{I}(\tau,-\mu,\phi)$, at an optical depth, τ, as an integration over all possible incident geometries at the top of the layer. The upward and downward matrices for light incident from below the layer are defined in a similar manner. The adding equations are used to determine $\mathbf{U}$ and $\mathbf{D}$.

If the light emerging from the layer is desired, either from the top or the bottom, then $\mathbf{U}$ and $\mathbf{D}$ are defined by their boundary values. These are the reflection and transmission matrices corresponding to light incident at the top of the layer:

$$\begin{aligned}\mathbf{T}(\mu,\mu',\phi-\phi') &= \mathbf{D}(\tau',\mu,\mu',\phi-\phi') \\ \mathbf{R}(\mu,\mu',\phi-\phi') &= \mathbf{U}(0,\mu,\mu',\phi-\phi')\end{aligned} . \tag{46}$$

The transmission and reflection matrices for light incident from below at the bottom of the layer are

$$\begin{aligned}\mathbf{T}^*(\mu,\mu',\phi-\phi') &= \mathbf{D}^*(0,\mu,\mu',\phi-\phi') \\ \mathbf{R}^*(\mu,\mu',\phi-\phi') &= \mathbf{U}^*(\tau',\mu,\mu',\phi-\phi')\end{aligned} . \tag{47}$$

The asterisk indicates light is incident from below. The optical depth of the entire layer is τ'. As before, the layer is divided into many layers of $\tau << 1$. If there is no reflecting surface and multiple scattering can be neglected, then the reflection and transmission matrices may be determined by these equations:

$$\mathbf{R}(\mu,\mu',\phi-\phi') = \frac{\varpi}{4(\mu+\mu')}\mathbf{Z}(\mu,\mu',\phi-\phi')\left\{1-\exp[-\tau'(\tfrac{1}{\mu}+\tfrac{1}{\mu'})]\right\} \tag{48}$$

and

$$\mathbf{T}(\mu,\mu',\phi-\phi') = \frac{\varpi}{4(\mu-\mu')}\mathbf{Z}(\mu,\mu',\phi-\phi')\left\{\exp[-\tau'(\tfrac{1}{\mu})]-\exp[-\tau'(\tfrac{1}{\mu'})]\right\} \qquad \text{if } \mu \neq \mu'$$

$$\mathbf{T}(\mu,\mu',\phi-\phi') = \frac{\varpi\tau'}{4\mu^2}\mathbf{Z}(\mu,\mu',\phi-\phi')\exp[-\tau'(\tfrac{1}{\mu})] \qquad (49)$$

The complete derivations are given in Hansen.[39] These approximated reflection and transmission matrices are now applied to the adding equations to calculate the reflection and transmission matrices of the combined layer. Notice the single-scattering properties.

The reflection and transmission matrices for the combined layer for light incident from above begin to be determined by the following relationships:

$$\mathbf{Q_1}(\mu,\mu',\phi-\phi') = \frac{1}{\pi}\int_0^{2\pi}\int_0^1 \mathbf{R}^*(\mu,\mu'',\phi-\phi'')\mathbf{R}(\mu'',\mu',\phi''-\phi')\mu''\,d\mu''\,d\phi''$$

$$\mathbf{Q_{n+1}}(\mu,\mu',\phi-\phi') = \frac{1}{\pi}\int_0^{2\pi}\int_0^1 \mathbf{Q_1}(\mu,\mu'',\phi-\phi'')\,\mathbf{Q}_n(\mu,\mu'',\phi-\phi'')\mu''\,d\mu''\,d\phi''$$

$$\mathbf{Q}(\mu,\mu',\phi-\phi') = \sum_{n=1}^{\infty}\mathbf{Q}_n(\mu,\mu',\phi-\phi') \qquad . \quad (50)$$

The matrix $\mathbf{Q}_1$, for the combined layer, is an integration of the reflection matrix of the bottom layer due to incidence from above, $\mathbf{R}$, times the reflection matrix of the top layer due to incidence from below, $\mathbf{R}^*$, over the appropriate solid angles for all possible multiple scattering contributions into the direction (μ,ϕ). Note that the two layers are identically homogeneous. The summation of $\mathbf{Q}$ adds all the repeated reflections (multiple reflections) between the two layers and n indicates the number of times the radiation crosses the combined layer going up. The prime indicates radiation coming from the top layer. The double prime indicates radiation from the bottom layer.

The multiple reflections contribute to the upward and downward propagation of radiation at any depth in the combined layer as

$$\mathbf{D} = \mathbf{T} + \mathbf{Q}\exp[-\tau_1(\tfrac{1}{\mu'})] + \mathbf{QT}$$

$$\mathbf{U} = \mathbf{R}\exp[-\tau_1(\tfrac{1}{\mu'})] + \mathbf{RD} \quad , \tag{51}$$

where this simplified notation has been implemented. Any product of matrices is actually the integration of the two matrices as in the form of the top equation in Eq. (50). It must be kept in mind that the bold quantities are matrices and matrix multiplication is not commutative.

Because layers 1 and 2 are identically homogenous, such that $\tau_1 = \tau_2$, the reflection and transmission matrices for the combined layer, $\mathbf{R}_c$ and $\mathbf{T}_c$, of optical depth $2\tau_1$ are finally found to be

$$\mathbf{R}_c(\mu,\mu',\phi-\phi') = \mathbf{R}(\mu,\mu',\phi-\phi') + \mathbf{U}(\tau_1,\mu,\mu',\phi-\phi') \times \exp[-\tau_1(\tfrac{1}{\mu})]$$
$$+\frac{1}{\pi}\int_0^{2\pi}\int_0^1 \mathbf{T}^*(\mu,\mu'',\phi-\phi'') \times \mathbf{U}(\tau_1,\mu'',\mu',\phi''-\phi')\mu'' d\mu'' d\phi'' \tag{52}$$

and

$$\mathbf{T}_c(\mu,\mu',\phi-\phi') = \mathbf{T}(\mu,\mu',\phi-\phi')\exp[-\tau_1(\tfrac{1}{\mu'})] + \mathbf{D}(\tau_1,\mu,\mu',\phi-\phi')\exp[-\tau_1(\tfrac{1}{\mu})]$$
$$+\frac{1}{\pi}\int_0^{2\pi}\int_0^1 \mathbf{T}(\mu,\mu'',\phi-\phi'')\mathbf{D}(\tau_1,\mu'',\mu',\phi''-\phi')\mu'' d\mu'' d\phi'' \quad . \tag{53}$$

The adding equations are further simplified by acknowledging the symmetries according to the phase matrix for a homogeneous layer.[43] The reflection matrices are

$$\mathbf{R}^*(\mu,\mu',\phi-\phi') = \mathbf{R}(\mu,\mu',\phi'-\phi) . \tag{54}$$

The transmission matrix, $\mathbf{T}^*$, can be related to the transmission matrix, $\mathbf{T}$, as

$$\mathbf{T}^*(\mu,\mu',\phi-\phi') = \mathbf{T}(\mu,\mu',\phi'-\phi) . \tag{55}$$

The above use of the doubling equations can be repeated for increasing depths of homogeneous layers until the desired optical depth is attained.

Truncation of the Scattering Matrix

The scattering phase function for atmospheric particulates is strongly peaked in the forward scattering direction, $\Theta = 0°$. For example, ice crystals have a forward peak five to six orders or more magnitude greater than the side or backward directions. This strong peak is due to diffraction of light. It is this peak that causes problems when trying to model cirrus clouds in radiative transfer.

Typically, in radiative transfer the phase function is expanded in Legendre polynomials. The Legendre expansion is particularly useful because the Legendre polynomials obey an addition theorem[37] and the expansion coefficients are determined using the Legendre polynomial orthogonality properties. The phase function defined by the addition theorem is applied to the radiative transfer equation. However, for ice crystals thousands of expansion coefficients are needed to properly represent the phase function. Using this many coefficients consumes much computing time and storage space.[44] Figure 11 displays the actual phase function, the phase function approximated by 250 coefficients, and the phase function approximated by 10000 coefficients. Obviously, using 10000 coefficients in a radiative transfer problem would not be practical.

Therefore, truncation is performed on the phase function to reduce the strength of the diffracted energy in the forward direction and hence reduce the number of expansion coefficients. The truncated method used is that developed by Hu et al.[45] referred to as δ-fit. This method is similar to the Delta-M method,[44] but uses a weighted least-squares fitting procedure to better approximate the phase function, especially at larger scattering

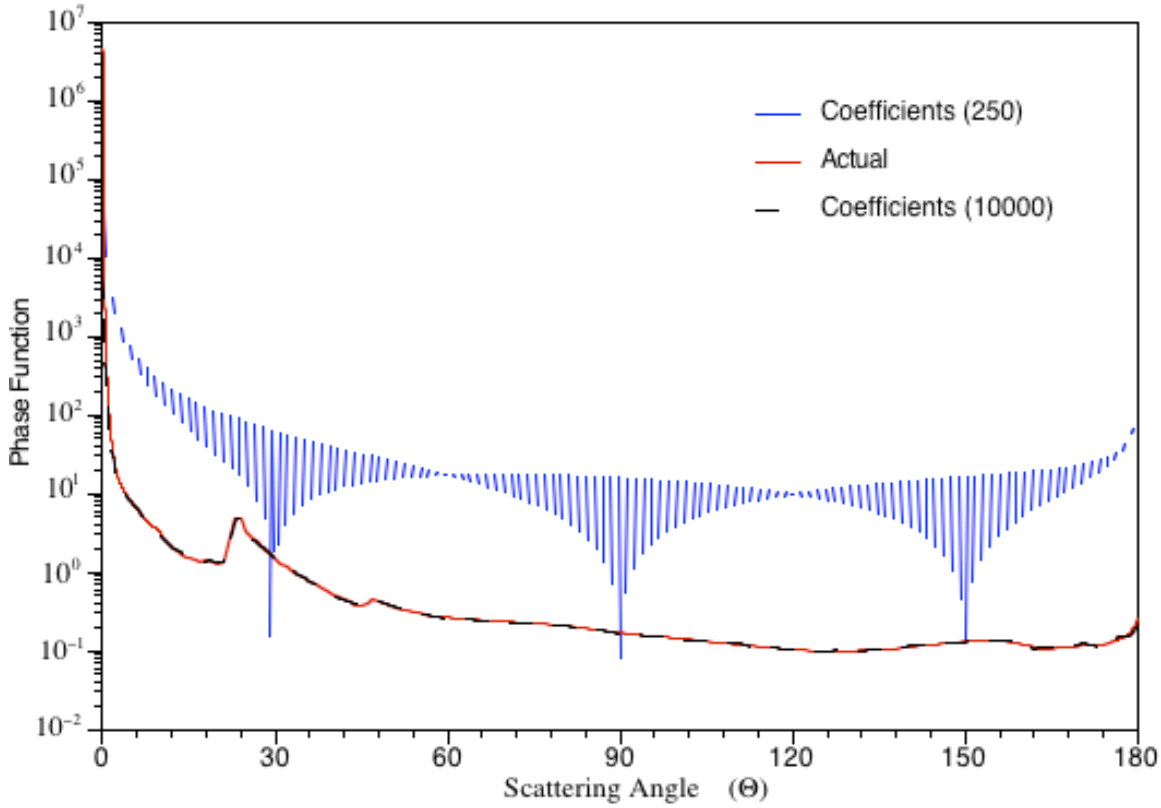

Fig. 11. Actual Phase Function to Expanded Phase Function. The blue line is the phase function expanded using 250 coefficients. The phase function expanded using 10000 coefficients approximates the actual phase function quite well. However, using thousands of coefficients in numerical calculations is very costly.

angles. The δ-fit method calculates the Legendre coefficients that best minimize the relative difference between the actual phase function and the approximate phase function.

Upon truncation of the phase function, the rest of scattering matrix elements must also be modified properly. Scaling the other elements preserves the degree of polarization. The other elements are scaled to the form that was used by Chami et al.[46] For example, $P_{22}(\Theta)$ becomes $P^{*}_{22}(\Theta)$ by using the expression

$$P_{22}^{*}(\Theta) = \frac{P_{22}(\Theta)}{P_{11}(\Theta)} P_{11}^{*}(\Theta) \tag{56}$$

where the asterisk, $*$, indicates the new scaled element. The other single-scattering properties also must be modified according to the similarity principle,[18,44] such that the properties of the system are altered equivalently. To obtain similar results as those for the case if the phase function had not been truncated, the single-scattering albedo and optical depth are scaled according to:

$$\varpi^{*} = \frac{(1-f)\varpi}{(1-\varpi f)}$$

$$\tau^{*} = (1-\varpi f)\tau \tag{57}$$

where f is the fraction of scattered energy due to the truncated peak. The truncated phase function and the other elements of the scattering matrix are now easily defined by less than 350 coefficients. From now on, the notation "scattering matrix" refers to the truncated scattering matrix.

Fourier Expansion

The adding-doubling method expands all functions dependent on the azimuth angle in a Fourier series. A Fourier expansion over the azimuth angle is applied to reduce the numerical computation time and storage space.[42] Specifically, by making these expansions the number of integrations are reduced.[23] The adding-doubling method requires the expansion coefficients of the scattering matrix as input. These expansion coefficients are input into the Fourier expansion to calculate the Fourier coefficients, for the phase matrix. For example, Haan et al.[23] expands the phase matrix into infinite sine and cosine series as

$$\mathbf{Z}(\mu,\mu',\phi-\phi') = \sum_{m=0}^{\infty}(2-\delta_{m0})[\mathbf{Z}^{cm}(\mu,\mu')\cos m(\phi-\phi') + \mathbf{Z}^{\mathrm{sm}}(\mu,\mu')\sin m(\phi-\phi')] \quad . \tag{58}$$

This method provides a way to examine each term independently.

Due to symmetry relationships[37] the expansion can be simplified and the Fourier coefficients $\mathbf{Z}^{cm}$ and $\mathbf{Z}^{sm}$ are related to the Fourier coefficient $\mathbf{Z}^{m}$. To determine the Fourier coefficients, $\mathbf{Z}^{m}$. an expansion method,

$$\mathbf{Z}^{m}(\pm\mu,\mu') = (-1)^{m}\sum_{l=m}^{\infty}\mathbf{P}_{m}^{l}(\pm\mu)\mathbf{S}^{l}\mathbf{P}_{m}^{l}(\mu) \quad , \tag{59}$$

is introduced involving, $\mathbf{P}_{m}^{l}$, which is the matrix composed of generalized spherical functions. The matrix $\mathbf{S}^{l}$ contains the expansion coefficients of the scattering matrix, $\mathbf{P}(\Theta)$. The superscript l denotes the degree of the polynomials in the generalized spherical functions. The generalized spherical functions are used to expand the scattering matrix and determine the expansion coefficients. Generalized spherical functions provide nice symmetry relationships and orthogonality properties. There use is particularly helpful when Stokes parameters and the scattering matrix are considered to be complex. They also have an addition theorem such that separation of variables may be applied. There is basis in their definition in angular momentum theory and they are discussed in greater detail in Hovenier and van der Mee.[37]

Validation (Rayleigh Scattering)

The code is validated with Coulson et al.[21] and also compared with results computed by a Monte Carlo code.[28] Coulson et al. [21] uses Chandrasekhar's formulation of the X and Y functions to calculate the reflected and transmitted polarized radiation due to Rayleigh scattering at the top and bottom of the layer, respectively. The results are

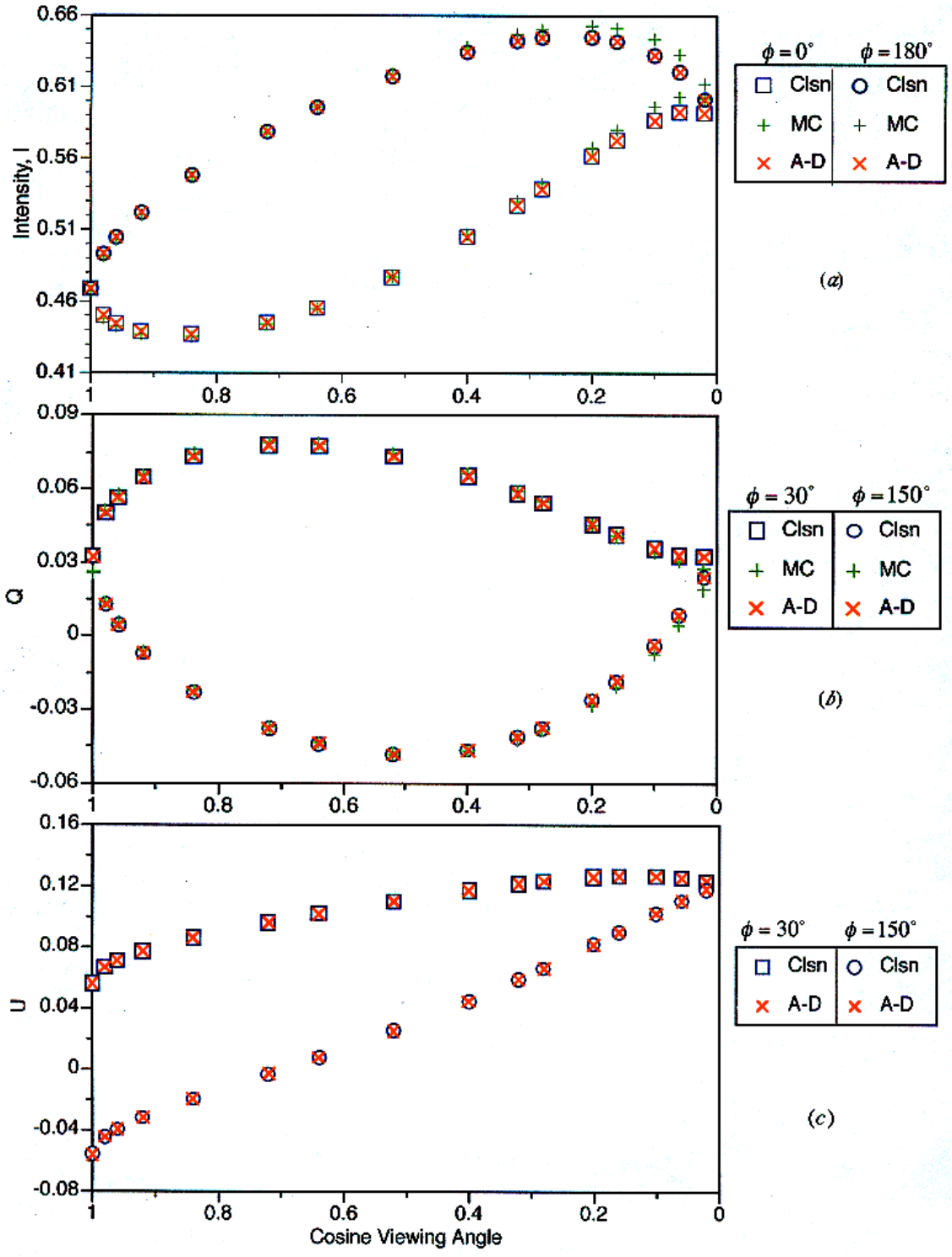

Fig. 12. Validation of Adding-Doubling Code. (a) The intensity of the reflected radiation at the top of the atmosphere at $\phi = 0^\circ$ and $\phi = 180^\circ$. (b)-(c) The Q and U parameters are viewed at the angles $\phi = 30^\circ$ and $\phi = 150^\circ$.

tabulated in the form of the Stokes parameters, I, Q, U, and the degree of polarization, P. The incident radiation is unpolarized solar radiation.

The results computed by the adding-doubling method compare extremely well with Coulson et al.[21] Figure 12 displays three graphs for the radiation measured at the top of the atmosphere. In the system there is a reflective Lambertian surface, such that the reflectivity, $A = 0.8$. The incident net flux of the solar energy is $\pi F_0 = \pi$. The optical depth of the system is $\tau = 1$. Finally, the incoming solar zenith angle is $\theta' = 53.13^\circ$. The Monte Carlo code by Hatcher[28] performs very well for the back scattering regions from $\mu = 1$ to approximately $\mu = 0.3$.

CHAPTER VI

RESULTS

The equations of the adding-doubling method are used to obtain the vector intensity of the light that is reflected out of the top of the layer. A detector resides above the layer and measures the intensity over many viewing angles, $(\theta, \phi - \phi')$, as depicted in Fig. 13. The reflection and transmission matrices are calculated within the code for all viewing angles and used to calculate the reflected Stokes parameters for each viewing angle. The incident Stokes parameters are normalized by the flux, F, of incident light which for this case $F = 1$. Therefore, the Stokes parameters actually become unit-less.

Some of the following figures display polar plots of the Mueller matrix. Figure 14 is an example of such a polar plot. The relative azimuth viewing angles $(\phi - \phi')$ are displayed from 0° to 360° and are measured in the counter-clockwise direction. The zenith viewing angles are measured in the radial direction such that $\theta = 0^\circ$ is at the center of the figure such that the detector is looking straight down. $\theta = 90^\circ$ is at the edge of the plot such that the detector is viewing in the horizontal direction. Actually, the polar plots are of the reduced Mueller matrix, where all elements, except M_{11}, are normalized by dividing by M_{11}.

There are four cases examined. The first case is for a mixed habit cirrus cloud. The habit percentages are those listed in Table 2. In the second case, three cirrus cloud layers are compared. Each cirrus cloud layer is composed of only one type of ice crystal. The comparison is made for the largest effective size of each habit. In the third case the effective sizes are compared for bullet rosette. Three effective sizes are considered. The fourth case examines the linear depolarization ratio for the different habits.

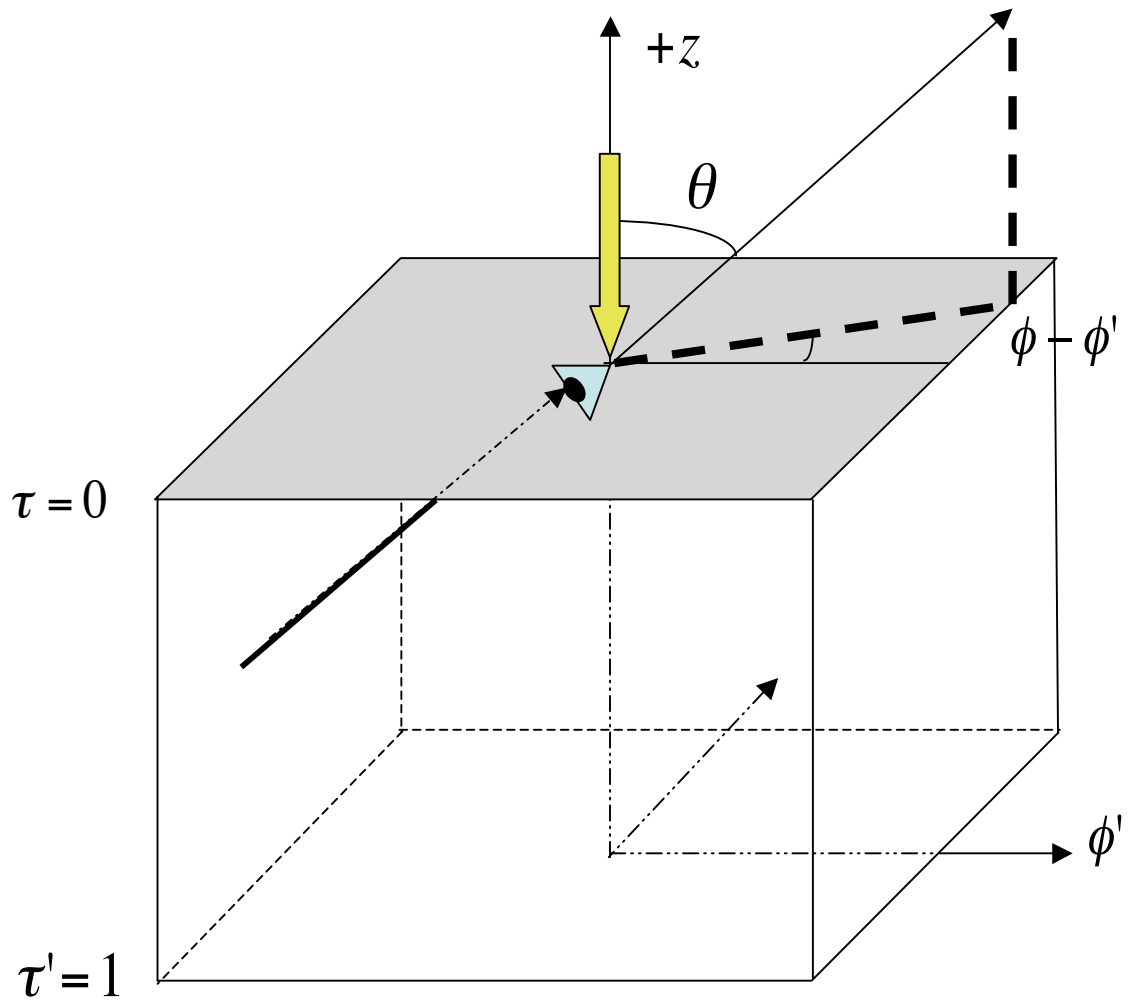

Fig. 13. Detector Viewing. In this example the incident radiation is at $\theta' = 0$. The radiation exiting at the top of the layer, viewed by the detector, is defined by the angles θ and $\phi - \phi'$. The incident radiation is that of a beam, everywhere incident at the top of the layer at $\theta' = 0$. Therefore, it is not a point source as the picture may advertise.

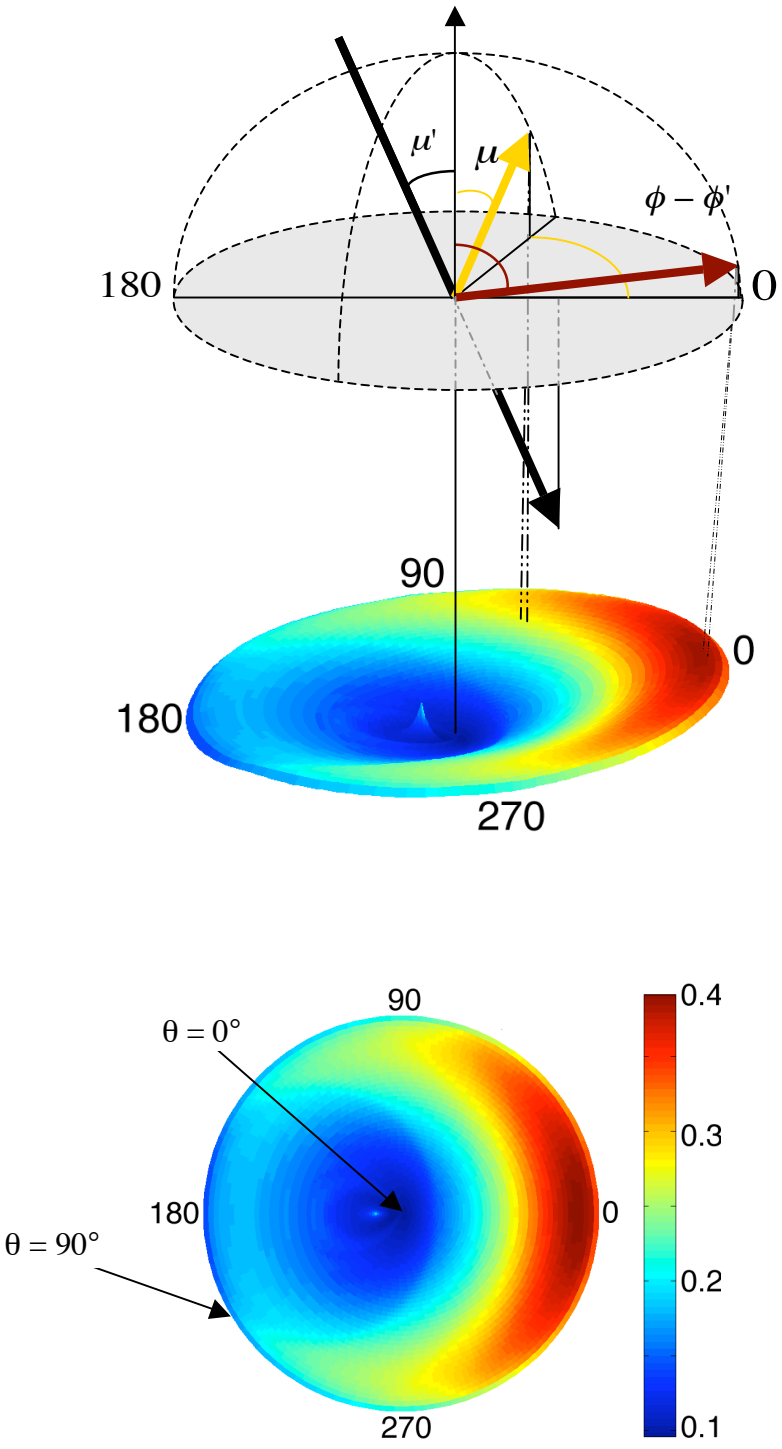

Fig. 14. Polar Plot Example of Mueller Matrix.

Case 1

A cirrus cloud of different habits with different percentages is displayed in Case 1. Table 3 lists the parameters of input to calculate single-scattering properties. Combining the habit percentages from Table 2, the size distributions, and the parameters in Table 3 give the average scattering matrix and bulk scattering properties. For this particular case, the largest effective size was studied. The doubling conditions in Table 3 give the properties of the cirrus cloud layer studied in Case 1.

Table 3. Case 1.

Single – Scattering Conditions	
Wavelength:	$\lambda = 0.532 \mu m$
Refractive Index:	$m_r = 1.311673$
Maximum Dimension:	L = 2μm to 3100μm
Doubling Conditions	
Albedo:	$\varpi = 1.0$
Optical Depth:	$\tau = 1.0$
Incident Zenith:	$\theta = 30^{\circ}$

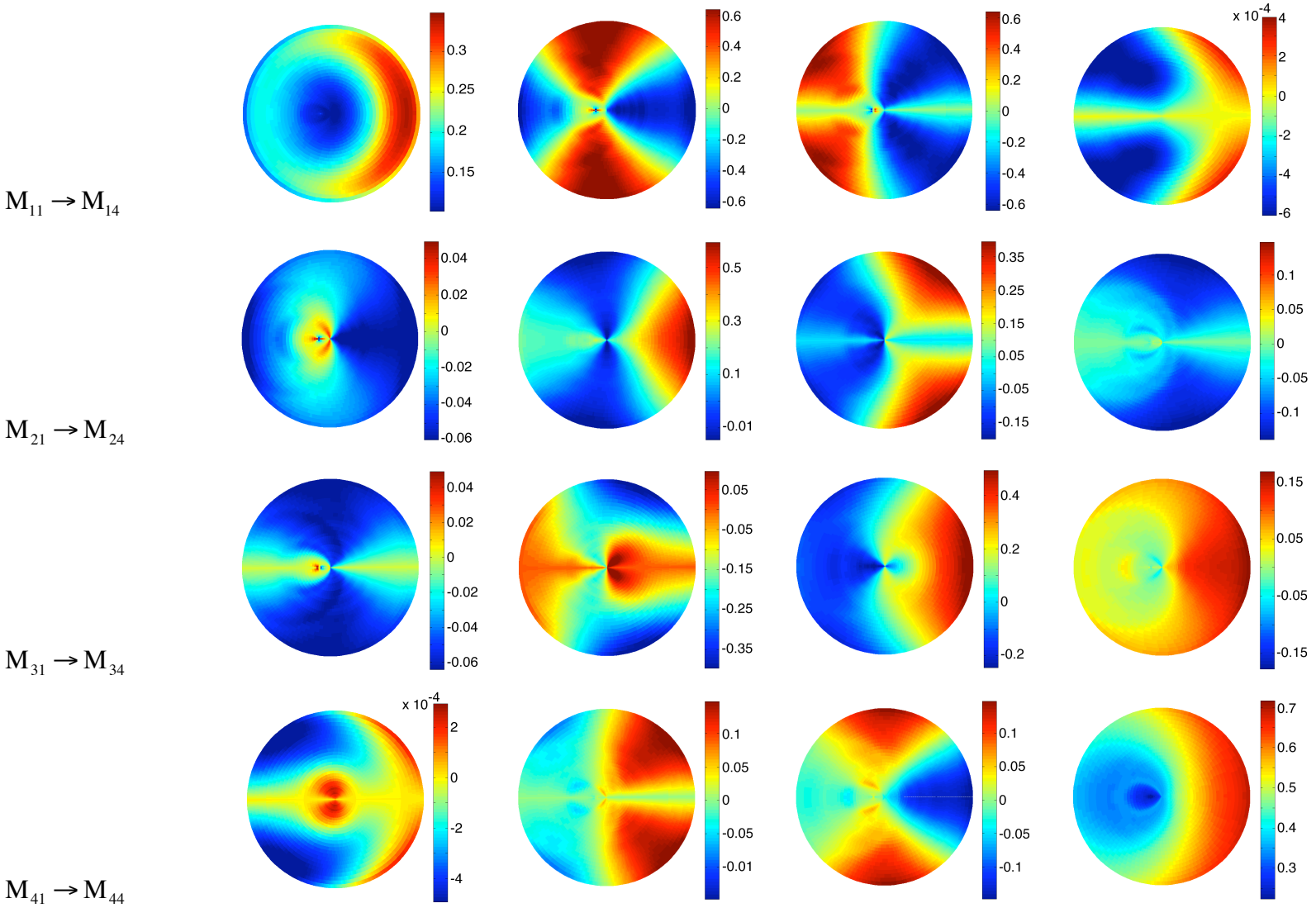

Fig. 15. Mueller Matrix for a Mixed Habit Cirrus Cloud. The Mueller matrix is for all orders of scattering at $D_e = 147.55 \mu m$.

Figure 15 is the 4×4 Mueller matrix computed for the mixed habit cirrus cloud. The first element of the Mueller matrix, M_{11}, is the element in the upper left hand corner. The rest of the elements follow from left to right and top to bottom. The Mueller matrix in Fig. 15 describes all orders of scattering that occur throughout the optical depth, $\tau = 1$. A slight peak is found at the viewing angle $(\theta = 30^{\circ}, \phi - \phi' = 180)$ for M_{11} that corresponds to the backscattering peak found in the scattering matrix at $\Theta = 180^{\circ}$. Figure 16 is the scattering matrix for Case 1.

The M_{44}/M_{11} element reflects the P_{44}/P_{11} elements of the scattering quite well. The smallest value near $(\theta = 30^{\circ}, \phi - \phi' = 180)$ is approximately found in the backscattering direction of P_{44}/P_{11}. The first and the last element of the reduced Mueller matrix is the easiest to understand using the scattering matrix, because they are not affected by the rotations of incident reference planes.

According to Hovenier and van der Mee[37] the phase matrix after two rotations of the reference plane contains zeroes in the upper right and lower left elements. The Mueller is proportional to phase matrix. However, the Mueller matrix in Fig. 15 is a product of multiple scattering contributions and is determined by incident light at $\theta' = 30^{\circ}$. Therefore, values found in the elements M_{14}/M_{11} and M_{41}/M_{11} are possibly due to a combination of multiple scattering and oblique incidence. Notice, these values are quite small and when compared to other cases of increased optical depth and/or incident angle they only vary slightly.

For the most part, the elements of the scattering matrix are relatively smooth. Of course, the major halo peaks of the phase function located at $\Theta \approx 22^{\circ}$ and $\Theta \approx 46^{\circ}$ are still apparent, although not as pronounced because of the presence of aggregates.

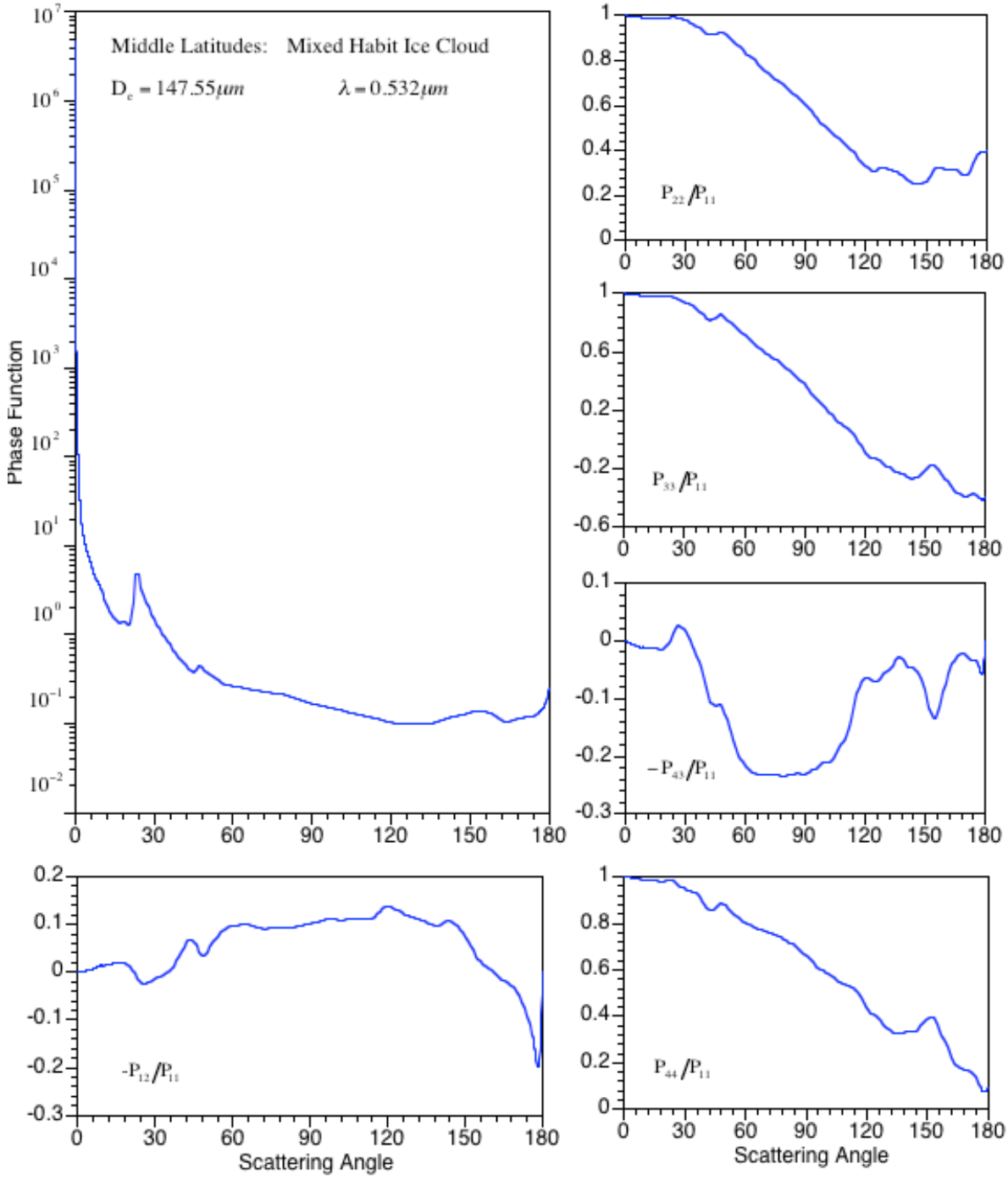

Fig. 16. Scattering Matrix for a Mixed Habit Cirrus Cloud.

The P_{33}/P_{11} element becomes less positive from the forward scattering angle to the backward scattering angle with a peak at $\Theta = 150^{\circ}$, similar to the one at P_{44}/P_{11}. This peak is described further by Takano and Jayaweera.[47] The values of $-P_{12}/P_{11}$ and $-P_{43}/P_{11}$ vary across the zero line, where $-P_{12}/P_{11}$ has a significant peak at $\Theta \approx 177^{\circ}$. This peak is described further in Case 2.

The elements of the reduced Mueller matrix provide information about the medium. In the next three cases, the sensitivity of the habit, effective size and optical depth is examined.

Case 2

In this case, each cirrus cloud layer is composed of only one type of habit. The sensitivity of the Mueller matrix due to these different habits can be observed by making comparisons. For each cirrus cloud layer, consider all properties to be the same, except for the scattering matrix that corresponds to each habit. Of course, the size distribution, which is the basis of comparison, must also be the same. However, due to the different volume to area ratio of each habit the effective sizes for the same size distribution will be different. Table 4 lists the conditions for this case. The size distribution number is an index for the distribution used. The smallest effective size is determined using the size distribution number of 1, and the largest is the size distribution number of 21.

Figure 17 displays several elements of the Mueller matrix for all orders of scattering for aggregate, bullet rosette, and plate. These elements were chosen because of their noticeable pattern difference between the habits. The values of the Mueller elements are proportional to the scattering matrix. By using Eq. (48), for calculating the single-

Table 4. Case 2.

Optical Depth: $\tau = 1$		Incident Zenith Angle: $\theta' = 0^\circ$	
Single-Scattering Albedo: $\varpi = 1$		Size Distribution Number: 21	
	Aggregate	Bullet Rosette	Plate
Effective Size, D_e	$231.79\mu m$	$91.99\mu m$	$100.25\mu m$

The effective size for each habit is different due to the different volume to area ratios of each habit. The other properties of the system are also listed.

scattering reflection matrix and Eq. (27), which computes the phase matrix, one sees the relationship between the scattering matrix and the Mueller matrix for single-scattering. For a system with incident radiation from $\theta' = 0^\circ$, the first rotation of the incidence reference plane to the scattering plane is along the azimuthal angle $\phi - \phi'$. In this particular case, the scattering plane is also the meridian plane of the scattered beam.

By using Eq. 27 and the azimuthal rotation, the phase matrix becomes

$$\mathbf{Z} = \begin{bmatrix} P_{11} & P_{12}\cos 2(\phi-\phi') & P_{12}\sin 2(\phi-\phi') & 0 \\ P_{12} & P_{22}\cos 2(\phi-\phi') & P_{22}\sin 2(\phi-\phi') & 0 \\ 0 & -P_{33}\sin 2(\phi-\phi') & P_{33}\cos 2(\phi-\phi') & -P_{43} \\ 0 & -P_{43}\sin 2(\phi-\phi') & -P_{43}\cos 2(\phi-\phi') & P_{44} \end{bmatrix}. \quad (60)$$

This phase matrix is proportional to the Mueller matrix for single-scattering. Because of this direct relationship, we will look at the single-scattering Mueller matrix compared to

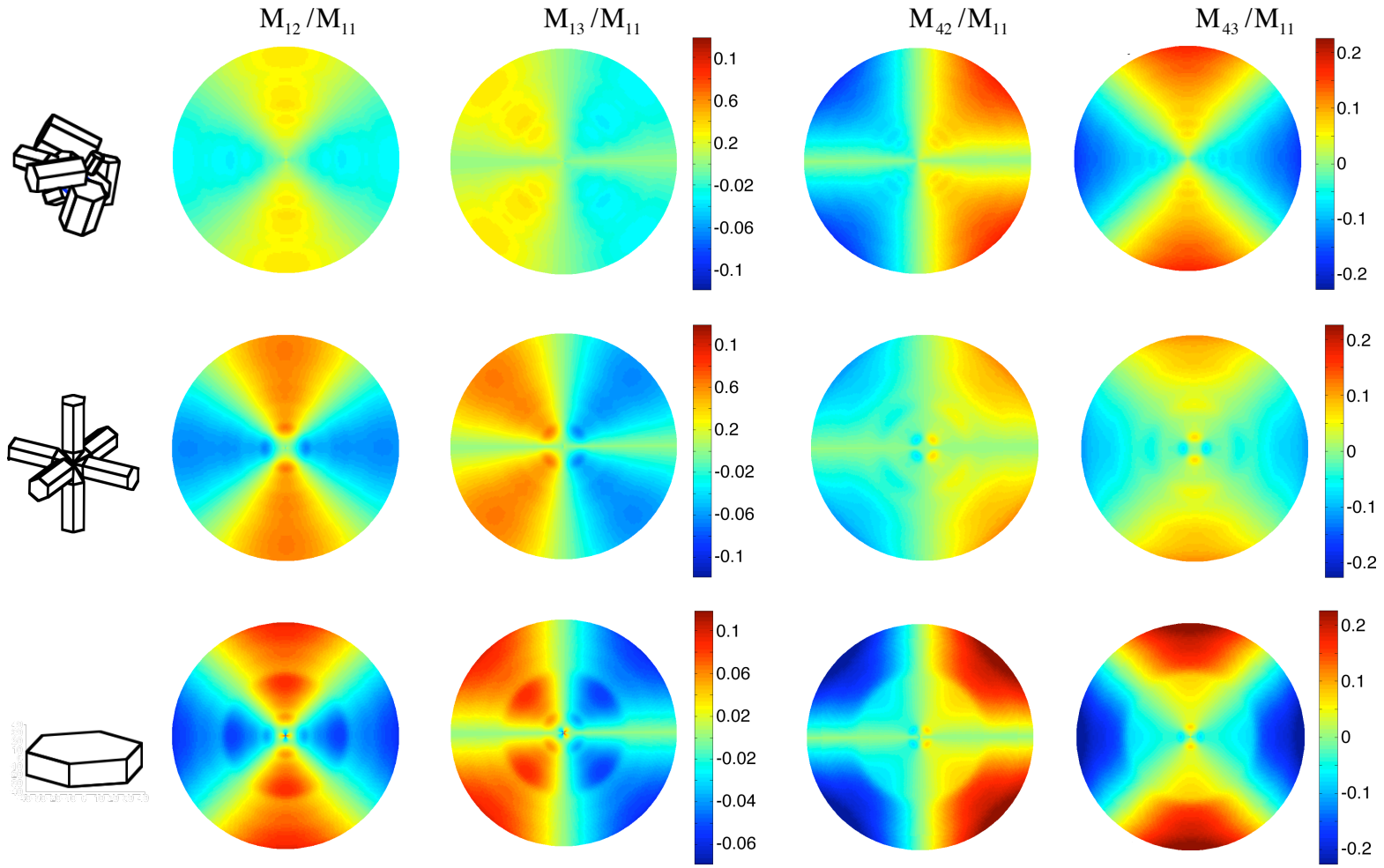

Fig. 17. Mueller Elements for All Orders of Scattering. The elements, M_{12}/M_{11}, M_{13}/M_{11}, M_{42}/M_{11}, and M_{43}/M_{11}. The patterns in these elements as compared for each habit reveal some noticeable differences.

the scattering matrix for the different habits. Figure 18, displays the $-P_{12}/P_{11}$ scattering element and M_{12}/M_{11}.

The patterns of M_{12}/M_{11} can be explained by the $-P_{12}/P_{11}$ element. There is a peak and consequently the largest polarization located at about $\Theta = 125^\circ$ of $-P_{12}/P_{11}$ for plate. This peak is not apparent in the other two habits. In the M_{12}/M_{11} element for plate, the broad peak of the highest value at $\phi - \phi' = 90^\circ$ is due to this peak. Also, there is a peak of high negative polarization of almost 50% for plate at $\Theta \cong 177^\circ$. This peak is not as strong for bullet rosette and is practically non-existent for aggregate. This peak, reviewed in Takano and Jayaweera,[47] comes from the amplitude scattering matrix of two types of rays, known as the near spatial skew rays and the near plane skew rays, for the near backscattering direction. The near spatial skew rays split upon interaction with the ice crystal and rotate reference planes, and the plane skew rays do not. The plane skew rays do not change the polarized direction. The first component, $|S_2|$ of the amplitude scattering matrix in the scattering plane becomes greater than $|S_1|$ due to the coordinate system rotation. From the derivation of the transformation matrix,[34] $-P_{12}/P_{11}$ is correspondingly negatively polarized.

Aggregate and bullet rosette have less of this feature because of their rough surfaces and the presence of branches, respectively. This peak is located at the center of M_{12}/M_{11} as a star-like pattern. Finally, at the 90° scattering angle, plate increase and bullet rosette actually decreases. Aggregate remains close to zero for the M_{12}/M_{11}, with only slight deviations.

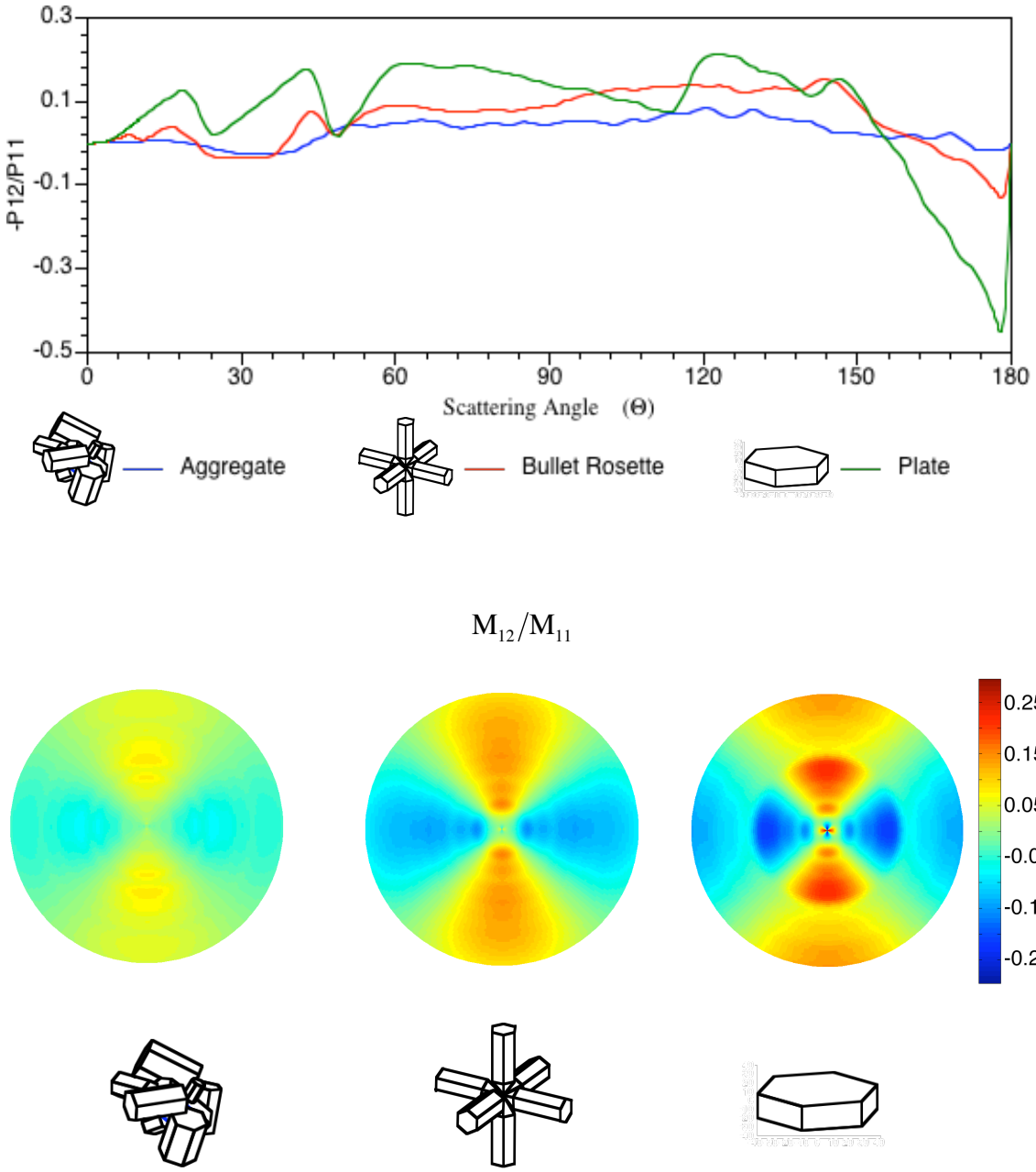

Fig. 18. Single-Scattering Mueller Element M_{12}/M_{11}. The scattering matrix element $-P_{12}/P_{11}$ compared to the Mueller matrix element M_{12}/M_{11}, for aggregate, bullet rosette, and plate. M_{12}/M_{11} depends on the azimuth direction and $-P_{12}/P_{11}$.

Figure 19 displays the $-P_{43}/P_{11}$ scattering element and M_{43}/M_{11}. There are some very interesting peaks below the 50° scattering angle associated with the 22° and 46° haloes, but we are only concerned about the scattering angles at and above 90°. In the $-P_{43}/P_{11}$ element, none of the habits significantly differ in polarization. However, the fluctuations of the peaks are different. The M_{43}/M_{11} element for the plate has two quite noticeable peaks in the azimuth direction of 90°, whereas bullet rosette and aggregate produce more fluctuations over a smaller scattering angle region. One major difference is the strength of polarization between the habits near the 90° scattering direction. Plate produces a polarization strength of ~40%. It seems possible to use the M_{43}/M_{11} element to distinguish between complicated geometry systems, such as aggregate, and less complicated systems, such as plate, by noting these fluctuations. Particularly between the scattering region of $\sim 120^{\circ}$ and 150°, aggregate has many minor peaks, whereas, bullet rosette has one negatively polarized peak, and plate remains quite smooth with no negatively polarized peak.

Finally, the P_{44}/P_{11} element and M_{44}/M_{11} are observed. There is no azimuthal dependence of the M_{44}/M_{11} element. The main characteristic to note is that plate is the only habit to have negative values of polarization. When considering circularly polarized incident light, the P_{44}/P_{11} element describes the handedness of the scattered electric field. So, if the values of P_{44}/P_{11} are negative, than the handedness of the scattered electric field will be opposite of the incident field. The P_{44}/P_{11} element, as are the other

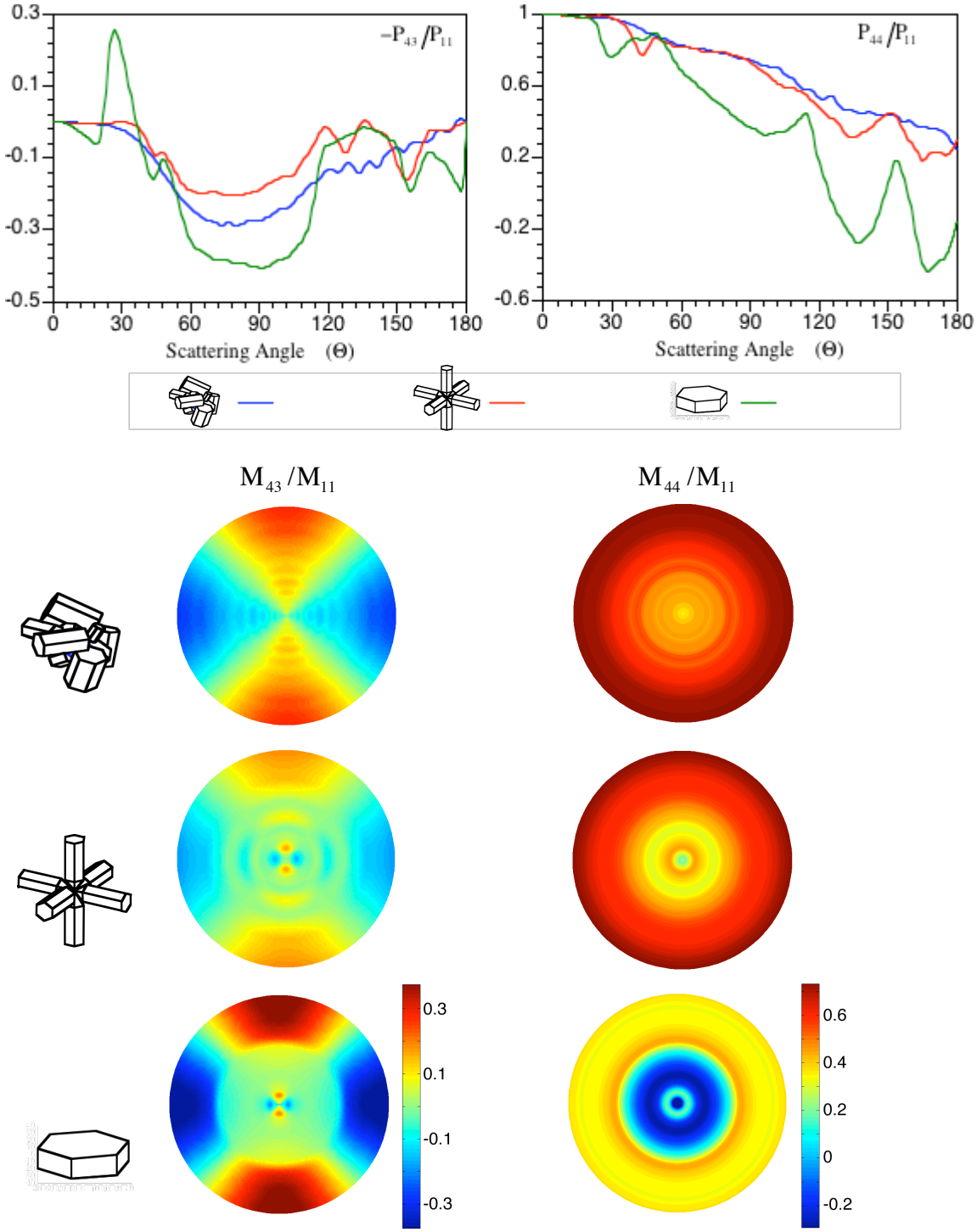

Fig. 19. The M_{43}/M_{11} and M_{44}/M_{11} Mueller Elements. The scattering matrix elements $-P_{43}/P_{11}$ and P_{44}/P_{11} are used to distinguish the features found in the Mueller element.

elements, comes from the product of the amplitude scattering functions[34,47] which are related to the Fresnel reflection coefficients. The negative values come from the opposite signed reflection coefficients due to the externally reflected rays of different incident angles less than the Brewster angle. The maxima at $\Theta \approx 155^{\circ}$ are due to three or more internal reflections.

By considering just these three elements of the single-scattering Mueller matrix, M_{12}/M_{11}, M_{43}/M_{11}, and M_{44}/M_{11}, it is possible to distinguish between habits when radiation is incident at $\theta' = 0^{\circ}$. The polarization values produced by plate mainly vary from the other habits in the location of peaks and the strength and existence of negative polarization. The very simple geometry of plate and its smooth symmetrical structure creates regions of strong peaks and minimal fluctuations. Bullet rosette for some angular regions, coincide with plate, but with smaller values of polarization. Takano and Liou[16] have noted the reduction of polarization across all scattering elements due to the reentry of rays into the branches of bullet rosette. This is noticeable in all elements of the scattering matrix. Finally, aggregate yields quite monotonic features, except that $-P_{12}/P_{11}$ displays many fluctuations of the polarization about zero. Also, the values for aggregate for M_{43}/M_{11} have many ripples that are probably due to the multiple reflections within aggregate. The rough surface of aggregate, which was initialized in the IGOM code, tends to 'wash out' any peak-like features and hence the curves for aggregate are rather smooth. These elements when used together provide a way to distinguish habits of complicated geometry.

Unfortunately, no information can really be deciphered from the multiple scattering elements of the Mueller matrix. The distinguishable patterns apparent in single-scattering are effectively smoothed over by multiple scattering. Therefore, using the total Mueller matrix, which includes all orders of scattering, to observe habit sensitivity is also difficult.

Case 3

In Case 3, similar to Case 2, each cirrus cloud layer is composed of only one type of habit. However, for this case a comparison is made for different particle sizes. Since, the scattering matrix is averaged over all crystal lengths for each number density we essentially compare particle effective sizes. Consider Table 5, which lists the conditions that went into the adding-doubling code for computation. For this case, we look at an incident angle of $\theta' = 30^{\circ}$. Bullet rosette is observed.

Table 5. Case 3.

Optical Depth: $\tau = 1$		Incident Zenith Angle: $\theta' = 30^{\circ}$	
Single-Scattering Albedo: $\varpi = 1$		Habit:	Bullet Rosette
Effective Size, D_e	$20.19\mu m$	$42.89\mu m$	$91.99\mu m$

The properties for a bullet rosette cirrus cloud.

Figure 20 displays the three size distributions used. Each effective size is produced by a different size distribution. The number index 6 contains crystals of maximum dimension exceeding 1000, but with very small density. The number index 21 produces the largest effective size because it has a larger number density for longer maximum lengths.

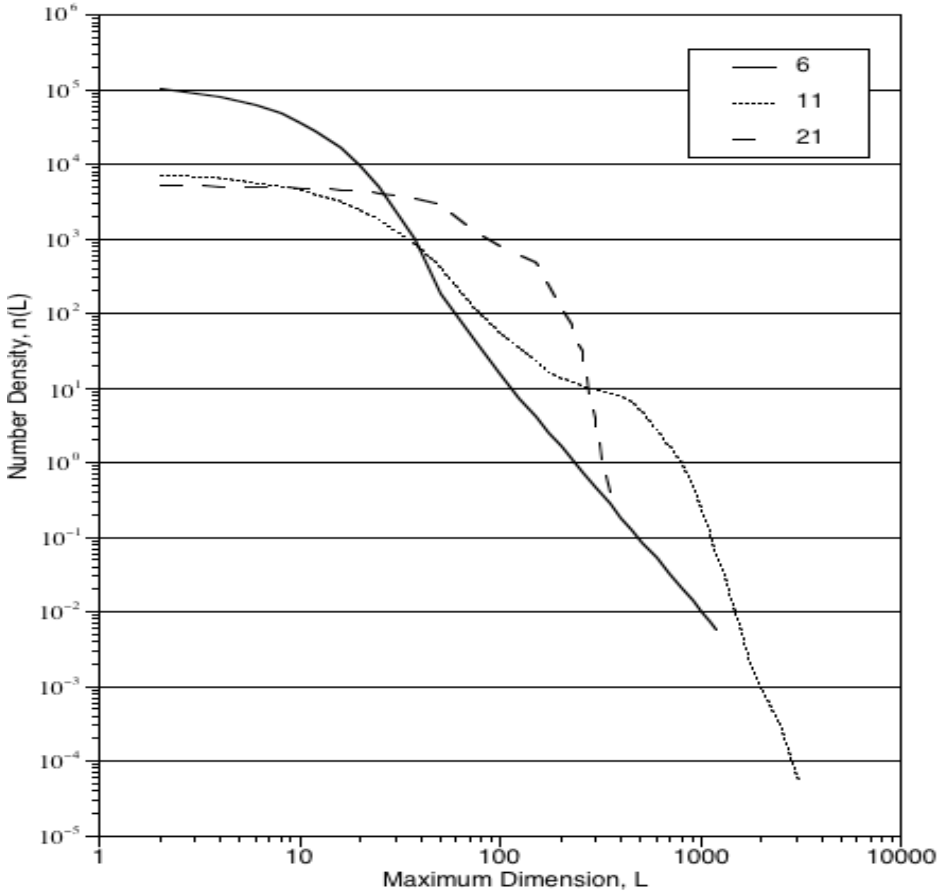

Fig. 20. Size Distributions. The size distribution index 6 corresponds to the smallest effective size and the index 21 corresponds to the largest effective size.

Figure 21 displays the scattering matrix for all three effective sizes for bullet rosette. The phase function is very similar for all three effective sizes. The only difference is that for $D_e = 20.19\mu m$ the peaks are not as sharp. However, more energy is diffracted in the forward scattering direction for $D_e = 91.99\mu m$. This intense diffraction, takes away energy from the other scattering directions. The main differences are found in the other elements of the scattering matrix.

In the $-P_{12}/P_{11}$ element, each size essentially produces the same patterns, except the strengths of polarization are different, where $D_e = 20.19\mu m$ generally produces the smallest deviating polarization values. The P_{22}/P_{11} element, is approximately similar, except for the backscattering angles. The same goes for the P_{44}/P_{11} element. Approximately, from the angles $165^\circ \leq \Theta \leq 180^\circ$, the peaks for each size vary in strength and location.

Both the single-scattering Mueller matrix and the total scattering Mueller matrix were calculated for this case. The Mueller matrix for all orders of scattering, does not yield much information about the different effective sizes for bullet rosette, i.e. the features found in the scattering matrix are harder to detect. Figure 22 compares the single-scattering Mueller matrix with the all orders of scattering Mueller matrix for the two largest effective sizes. The patterns are quite similar, but notice the 'star-like' patterns for the single-scattering Mueller are definitely distinguishable from the all

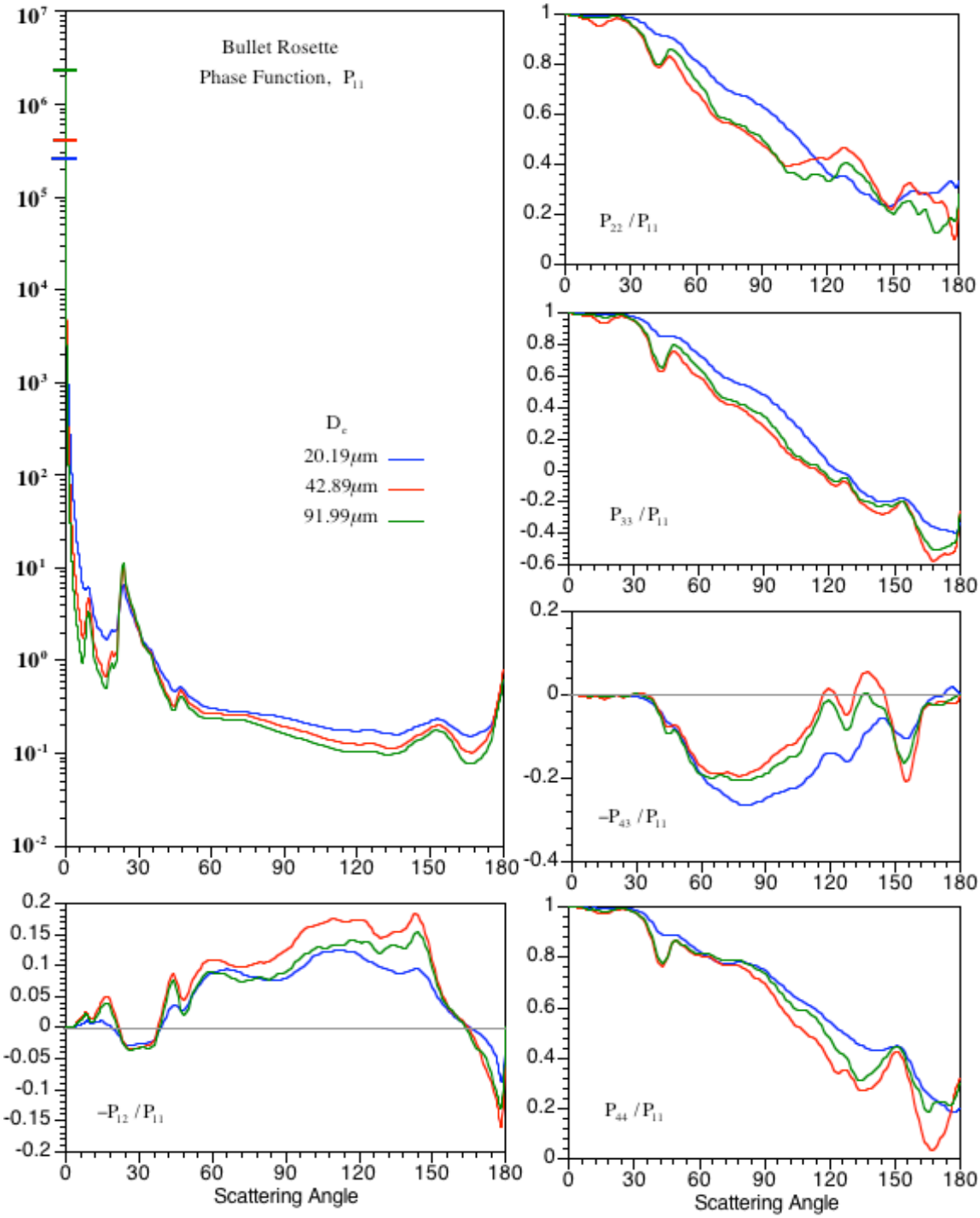

Fig. 21. Scattering Matrix for Bullet Rosette. The three effective sizes are quite similar, particularly for the phase function. The other elements show small deviations.

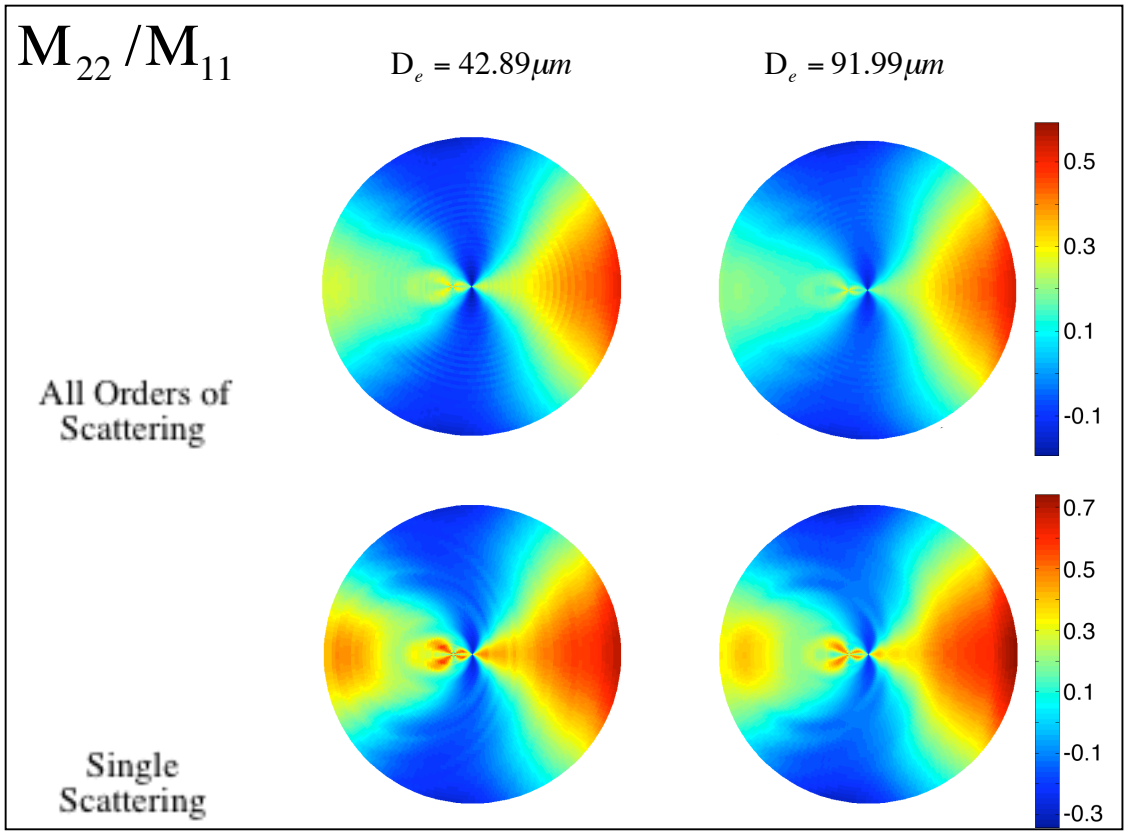

Fig. 22. Mueller Element M_{22}/M_{11} for All Orders and Single-Scattering. The top row is for all orders of scattering and the bottom row corresponds to single-scattering.

orders of scattering Mueller matrix. The Mueller matrix for all orders of scattering includes all multiple scattering that occurs in the layer, whereas the single-scattering Mueller is just the first reflection of the top of the layer into the detector. Therefore, the single- scattering Mueller matrix will be used here, for further analysis.

Now, consider some elements of the single-scattering Mueller matrix for $D_e = 20.19\mu m$ and $D_e = 91.99\mu m$. The patterns of the scattering matrix are easily distinguishable in the M_{11} and M_{44}/M_{11} elements (Fig. 23). This is a consequence of their invariance from the rotations of the reference planes. However, due to the changing incident zenith angle, these elements now depend on the relative azimuth. In M_{11}, a strong peak is located at $\theta = 30^\circ$ which is associated with the backscattered intensity of the phase function at $\Theta = 180^\circ$. The maximum values at $\theta = 90^\circ$ and $\phi - \phi' = 0^\circ$ are from the increasing intensity values going from $\Theta \approx 135^\circ$ to 90°. The circular polarization element M_{44}/M_{11} noticeably follows the P_{44}/P_{11} element, as well.

M_{23}/M_{11} and M_{32}/M_{11} are affected by the rotations of the reference planes and are dependent on both P_{22}/P_{11} and P_{33}/P_{11} of the scattering matrix. In M_{23}/M_{11}, there are peak patterns occurring in the backscattering direction at the viewing angle of $\theta = 30^\circ$, which occur for the larger effective size. There are larger values of polarization found for $D_e = 20.19\mu m$ in the near side scattering regions where the relative azimuth is approximately $280^\circ - 320^\circ$ and $40^\circ - 80^\circ$. In general, from $\Theta = 0^\circ \sim 110^\circ$ the smaller effective size exhibits more positive values of polarization for both elements. However, throughout all elements, except $-P_{43}/P_{11}$, $D_e = 91.99\mu m$ varies more in the values of polarization. I would anticipate this is due to more internal reflections occurring within larger particles.

Nothing has been said about the other two habits and their polarization values due to each effective size. Aggregate produces almost no differences in polarization as

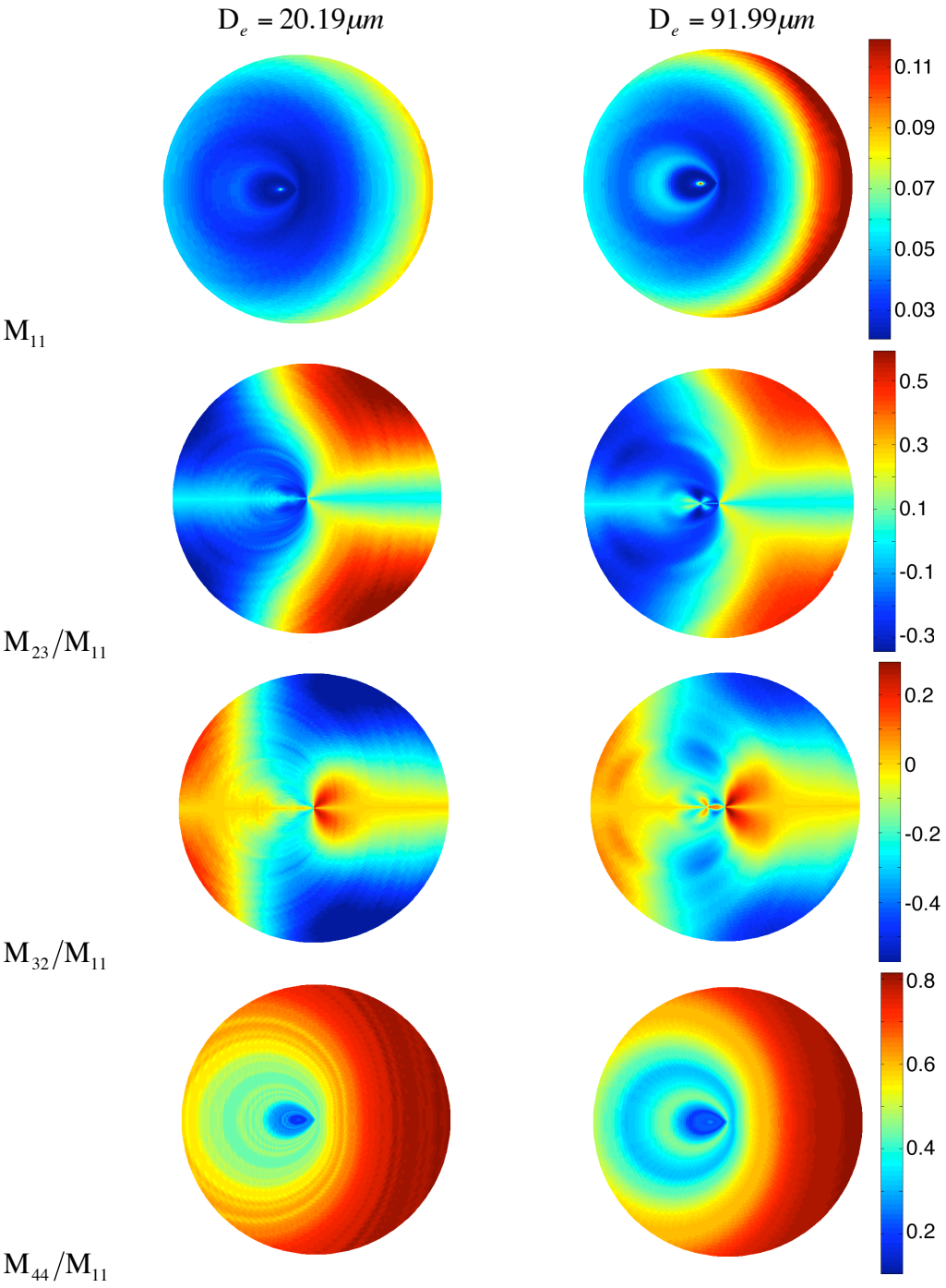

Fig. 23. Mueller Elements for Single-Scattering Bullet Rosette.

viewed in the Mueller matrix, which is expected when comparing the scattering matrices of each effective size. They are almost identical. This can be attributed to the rough surface of aggregate and its complex internal reflections, virtually eliminating any distinguishing features.

Plate is quite similar to bullet rosette. Except for the strength of the intensity and polarization, the first and last elements are almost identical, and the other two elements compared in Fig. 23 for plate differ in the same regions as bullet rosette. Comparing effective sizes for a specific habit does not yield much information about their sizes. However, this is only a minute representation of the of all the possible size distributions. Therefore, this may not be the case for all effective sizes. Of course, considering random orientation and even averaging over size distribution eliminates some determining features unique to some crystal sizes.

Case 4

Now, we will take a look at the depolarization ratio for the three different habits. The depolarization ratio is obtained through lidar measurements and is a useful technique to distinguish between water and ice clouds.[18] Particularly, we would like to show the differences in the different habits for single-scattering. The depolarization ratio, δ, is

$$\delta = \overline{P}_{\perp} / \overline{P}_{//}, \tag{61}$$

where $P_{\perp}$ and $P_{//}$ represent the perpendicular and parallel components of power with respect to the source axis.[48] The source emits either a vertically or horizontally polarized

beam so that the measured perpendicular component is perpendicular to the orientation of the emitted beam and the parallel component oscillates in the same direction as that of the emitted beam.

The depolarization ratio is basically a measure of how much linear polarization is being modified due to interactions with some medium. In theory, spherical water droplets should produce ratio values equal to zero, but observations reveal values near zero.[48] At the incident angle $\theta' = 0^\circ$, for ice crystals, ratio values near the forward scattering direction are zero and typically range between zero and one for all other scattering angles.

The depolarization ratios are computed here by considering the two incident states of polarization. First, consider the incident Stokes parameters of $(1,1,0,0)$, where the incident electric field oscillates only along the axis of the source, and corresponds to Fig. 7(h). In this case, consider the axis to be the horizontal component. The depolarization ratio δ_h, where the incident is only along the horizontal component, can be defined using the scattered Stokes parameters as calculated from the incident Stokes parameters $(1,1,0,0)$ as

$$\delta_h = \frac{\mathrm{I_s} - \mathrm{Q_s}}{\mathrm{I_s} + \mathrm{Q_s}}, \tag{62}$$

where the subscript (s) denotes the scattered parameters. This can be reduced further to truly understand how the electric field components are involved by considering the definition of the Stokes parameters in Eq. (18), such that Eq. (62) becomes

$$\delta_h = \frac{E_\perp E_\perp^*}{E_{//} E_{//}^*}. \tag{63}$$

Consequently, Eq. (63) is truly a measure of the intensity in the perpendicular direction to the intensity in the parallel direction. By using Eq. (33) and Eq. (38), Eq. (62) becomes

$$\delta_h = \frac{P_{11} - P_{22}}{P_{11} + 2P_{12} + P_{22}}, \tag{64}$$

where the depolarization ratio is dependent on the scattering elements. This equation describes the depolarization of the incident beam from the incident parallel direction due to single-scattering.

Second, consider the incident Stokes parameters of $(1,-1,0,0)$, where the incident electric field oscillates corresponding to Fig. 7(g). In this case, consider the axis to be the vertical component. The depolarization ratio δ_v, where the incident is only along the vertical component and has the incident Stokes parameters $(1,-1,0,0)$ is defined as

$$\delta_v = \frac{I_s + Q_s}{I_s - Q_s}. \tag{65}$$

The linear depolarization ratio, δ_v, is expressed by the scattering elements as

$$\delta_v = \frac{P_{11} - P_{22}}{P_{11} - 2P_{12} + P_{22}}. \tag{66}$$

Consider the scattering matrix for three habits, aggregate, bullet rosette, and plate. Figure 24 displays all three habits for the largest effective size. The effective sizes correspond to those used in Case 2. The depolarization ratio, δ_h, decreases for plate from

$\sim 120^{\circ}$ to 177° and makes a drastic increase and finally peaks at 180°. These features were discussed in Case 2. The depolarization ratio, δ_v, closely matches δ_h in the forward scattering region. The backscattered linear depolarization ratio for both δ_v and δ_h is smaller for plates than for the other two habits. These ratios were discussed in Takano and Jayaweera,[47] and seem to come from the difference in backscattered symmetrical skew rays and plane skew rays. Plate has more plane skew rays that are backscattered than symmetrical spatial skew rays. The plane skew rays do not rotate upon interaction with an ice crystal and therefore are reflected in the backscattering direction with the same electric field orientation. Bullet rosette and aggregate have a more complicated geometry such that plane skew rays are not as abundant causing stronger depolarization. Also, with more internal reflections possible, due to the bullet rosette branches, there is greater depolarization. The depolarization ratio curve for aggregate is quite smooth because of the rough surfaces. The bottom graph of Fig. 24 is the difference, $\delta_h - \delta_v$, in the two linear depolarization ratios. Notice for most scattering angles bullet rosette has the greatest difference. Aggregate shows minimal differences, which can be attributed to the complex structure of aggregate. Aggregate does not produce dominating depolarization values for either ratio. Both ratios are almost equally determined by the complex internal ray paths due to internal reflections: such that neither symmetrical spatial skew rays nor plane skew rays dominate to give peak features.

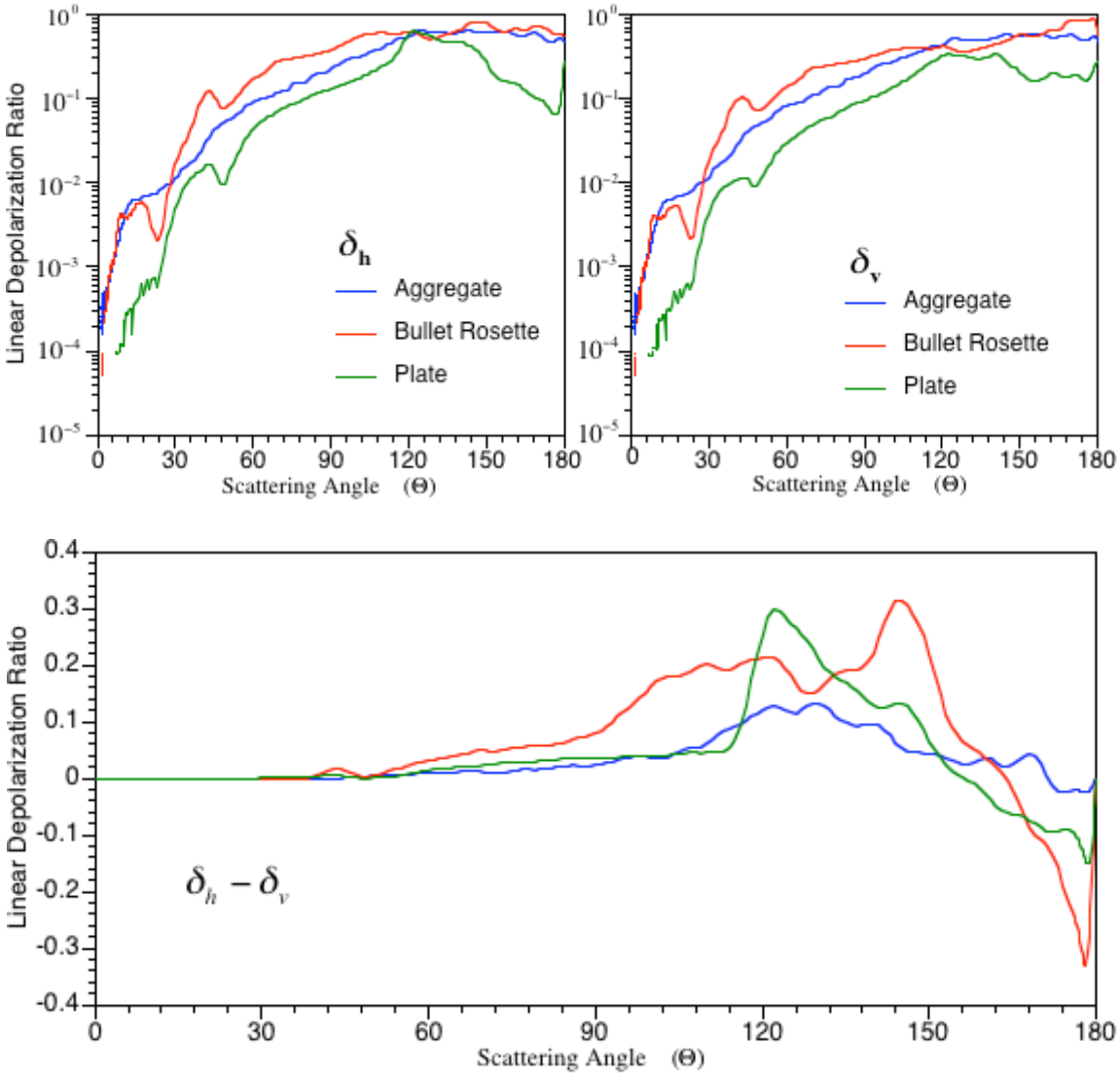

Fig. 24. Habit Depolarization Ratios. The graph on the left (right) is the ratio of the measured vertical (horizontal) component to the measured horizontal (vertical) component, where horizontally (vertically) polarized light is incident. The depolarization ratio is highly dependent on scattering angle. The bottom graph displays the difference, $\delta_h - \delta_v$, of the top two graphs. This graphs shows a strong dependence of the polarization of light with respect to habits.

In the top graphs, the depolarization ratio for plate reveals a sharp decrease near the backscattering angle $\Theta = 178^{\circ}$, associated with the backscattered skew rays. This feature is found in the scattering element $-P_{12}/P_{11}$ for aggregate and bullet rosette, but is not obvious in these graphs. The bottom graph confirms this feature. Also, the bottom graph clearly distinguishes the peaks at $\Theta \approx 125^{\circ}$ for plate and $\Theta \approx 150^{\circ}$ for bullet rosette.

This method, $\delta_h - \delta_v$, closely resembles the $-P_{12}/P_{11}$ element. The $-P_{12}/P_{11}$ element and $\delta_h - \delta_v$ are graphed together in Fig. 25 to show their resemblance. It is interesting to note that $\delta_h - \delta_v$ follows quite close to $-P_{12}/P_{11}$ for the side and back scattering directions. It does not follow the pattern in the forward directions because diffraction of the ice crystal dominates over internal reflections, therefore yielding similar values for both linear depolarization ratios and hence giving zero.

If both depolarization ratios can be calculated, then this method may be applied. By matching the correct $-P_{12}/P_{11}$ element to this difference in depolarization ratios gives a very useful way to determine particle shape. The increase in the depolarization values in the side and backward directions come from multiple scattering events within the ice crystal which dominant over the forward diffraction.[48]

It is obvious just from these graphs that polarization of the scattered beam is dependent on habit. Lidar provides a method for determining these polarization differences and consequently distinguishing particle shape, particularly, in the side and back scattering regions of $90^{\circ} < \Theta \leq 180^{\circ}$.

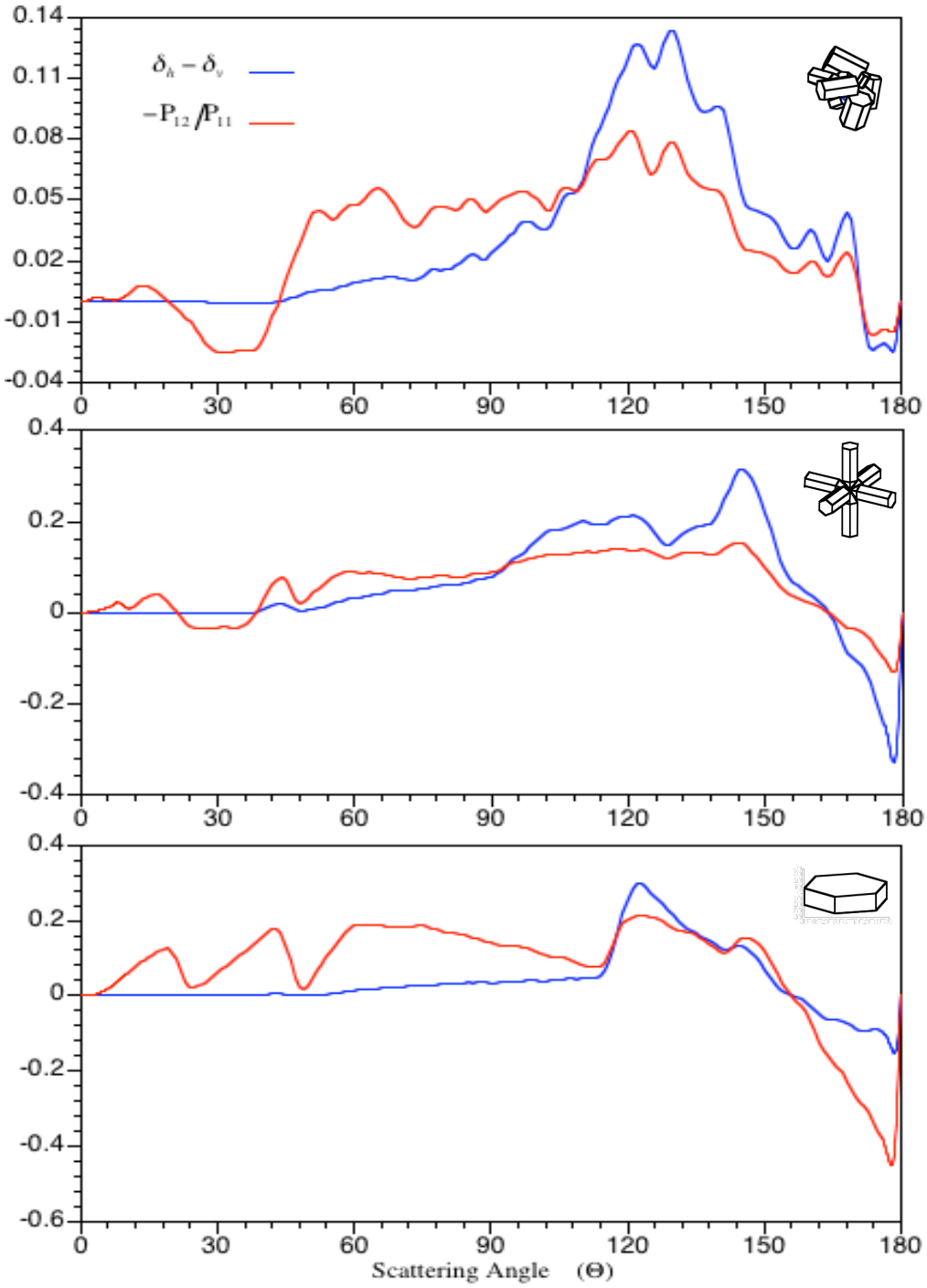

Fig. 25. Depolarization Ratios with Linear Degree of Polarization. The subtraction of the linear depolarization ratios gives a pattern that closely resembles $-P_{12}/P_{11}$ for each habit.

In Case 3, an attempt was made to distinguish ice crystal effective size for bullet rosette. Figure 26 is the same as Fig. 24 but comparing the different effective sizes for bullet rosette. Unfortunately, the three effective sizes displayed in this form give us no more information.

Now, consider the scenario where a cirrus cloud of some optical depth is viewed from directly overhead, so that scattering angles are between 90° and 180°. We can compare the depolarization ratios above for different optical depths to understand how multiple scattering effects the polarization. This method cannot be compared to that used by lidar. Lidar is a point source, whereas, the depolarization ratios determined from the adding-doubling code come from a beam of light. However, a comparison is still made between different optical depths using the radiative transfer code.

In Fig. 27, a thin ice crystal layer, only contributing to single-scattering, and an ice crystal layer of optical depth, $\tau = 1$ are compared for aggregate, bullet rosette and plate. As expected, the increasing optical depth causes linear depolarization to increase. Increased internal reflections in an ice crystal cause increased depolarization ratios as is apparent by the dependence of the depolarization ratio on the scattering angle (Fig. 27). Now, multiple scattering throughout the cirrus cloud layer, analogous to increased internal reflections, increases the linear depolarization ratios.

For all cases, linearly polarized radiation is incident at $\theta' = 0$. Notice, the depolarization ratios for the increased optical depths approximately parallel the single-

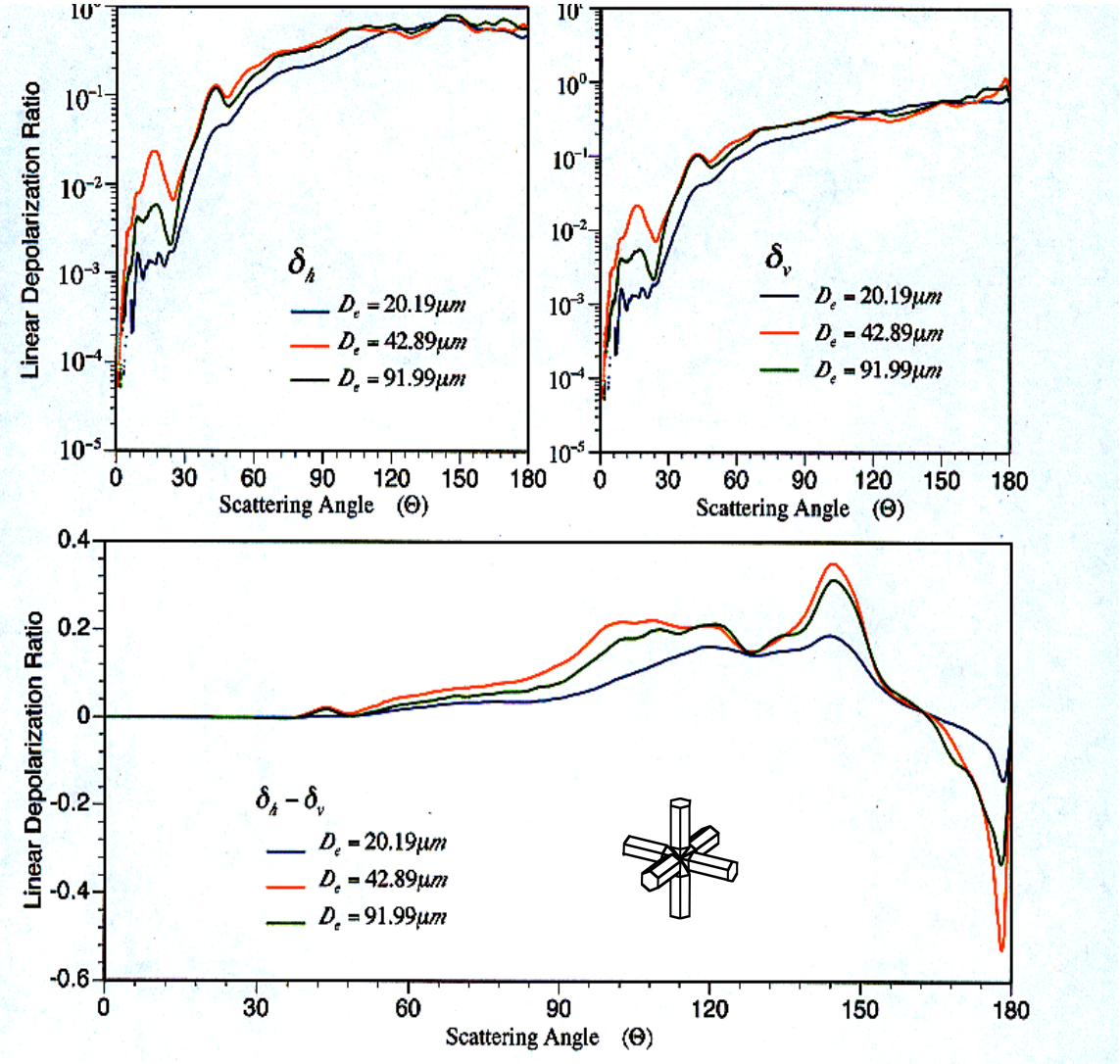

Fig. 26. Depolarization Ratios for Three Effective Sizes. Three effective sizes for bullet rosette are compared. No absolutely indistinguishable differences between effective sizes are observed.

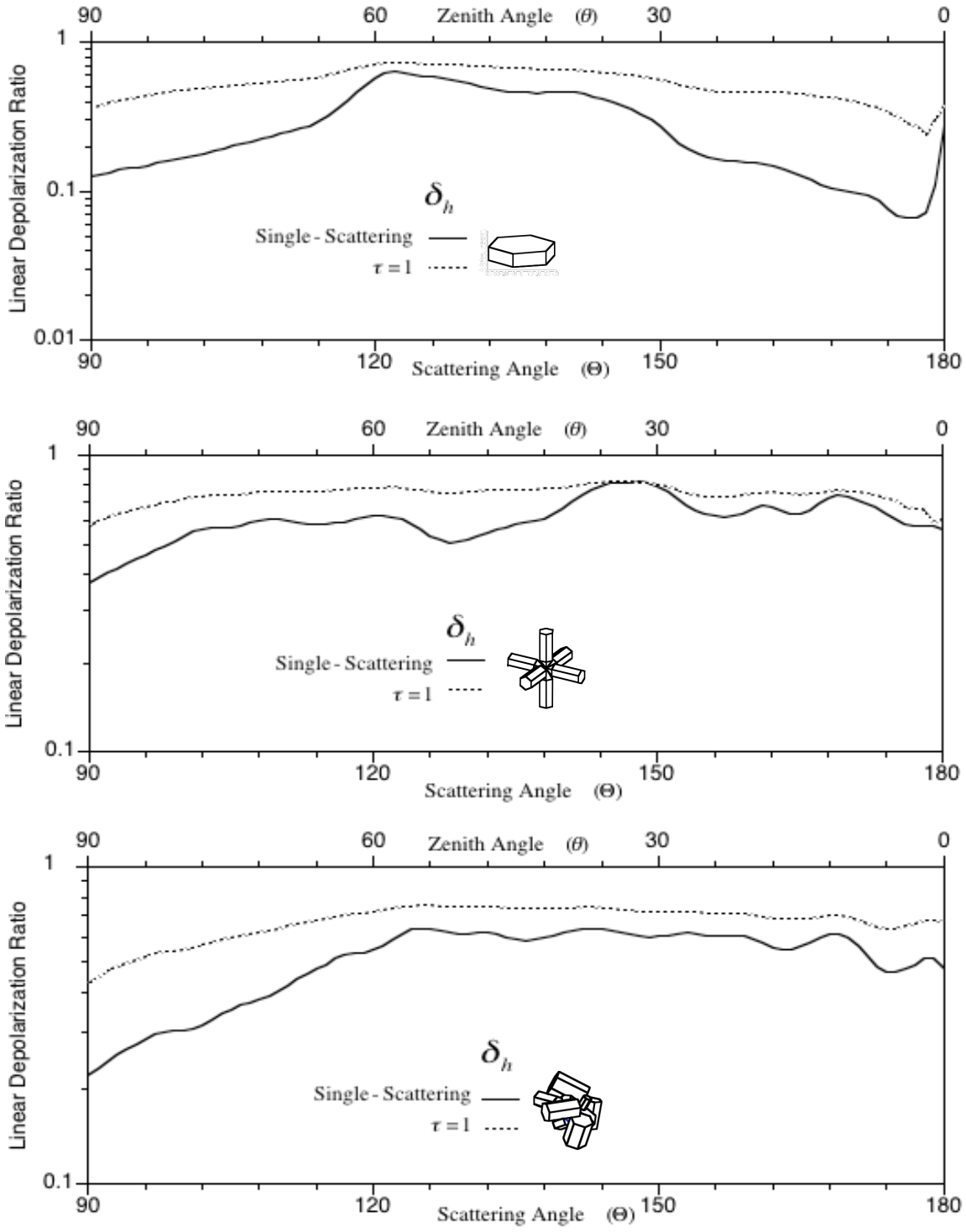

Fig. 27. Depolarization Ratios and Optical Depth. The depolarization ratio increases for increasing optical depth for all habits.

scattering depolarization ratios. However, the distinct peak features that occur in the single-scattering cases for all habits are smoothed over by the increase in multiple scattering in the layer. With more reflections throughout the layer, and consequently more rotations of the incident reference plane per reflection, the incident beam becomes more depolarized.

Again, Fig. 28 confirms the dependence of the linear depolarization ratio on the optical depth. For $\tau = 5$, linear depolarization values exceed those for $\tau = 1$ and single-scattering. The features due to single-scattering are less evident for $\tau = 1$ and are completely indistinguishable for $\tau = 5$. For all cases, the depolarization ratio increases with increasing optical depth.

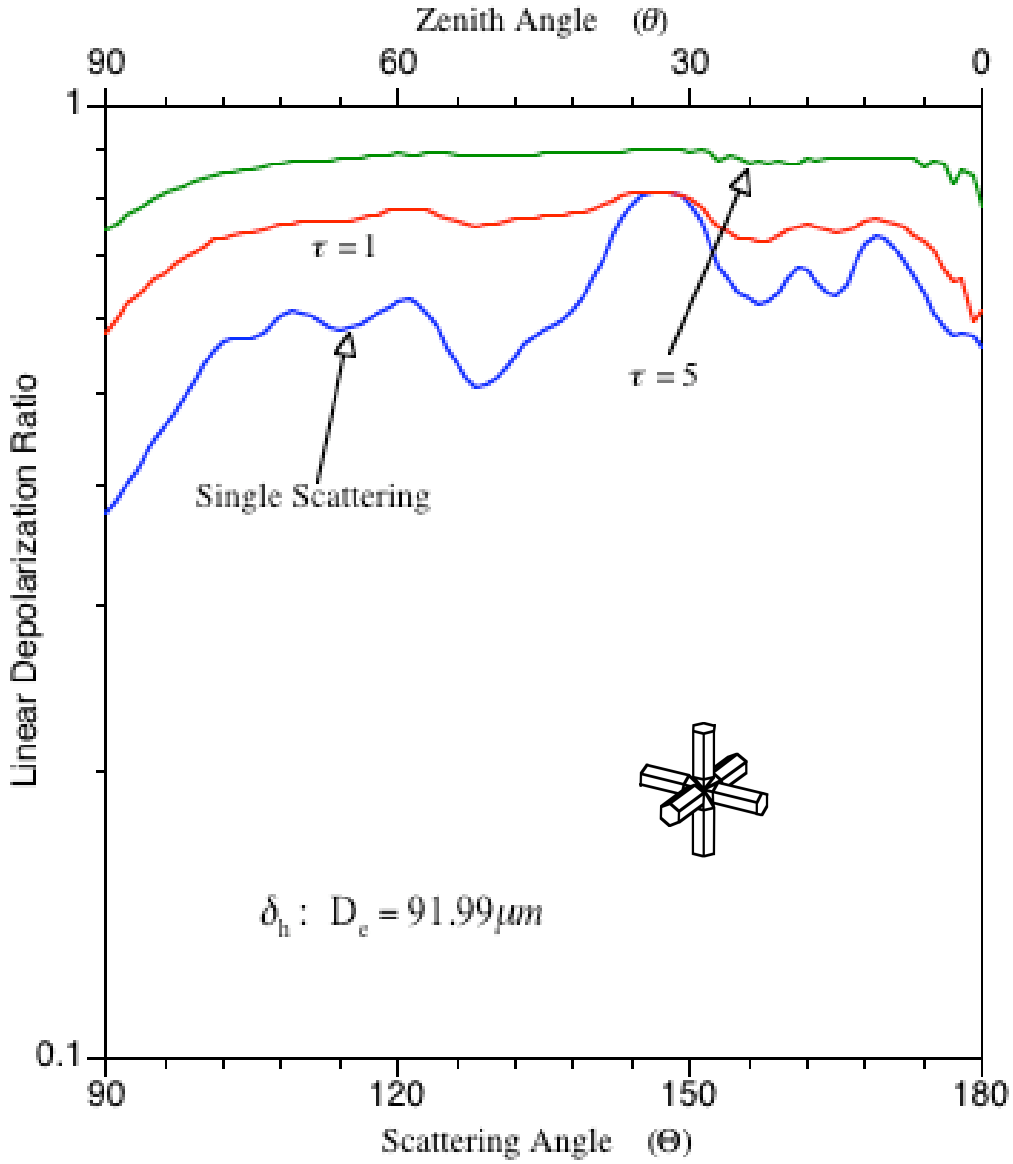

Fig. 28. Depolarization Ratio for Different Optical Depths: Bullet Rosette.

CHAPTER VII

SUMMARY

Polarization has been included in the solution of the scattered radiation field due to interaction with a cirrus cloud. An adding-doubling method, particularly the doubling method, was used to determine the reflected Stokes parameters at the top of the cirrus cloud layer. Four polarization states of incident light were introduced into the cirrus cloud layer. These four polarization states are related to the measured scattered Stokes parameters by the Mueller matrix, which completely describes the properties of the cirrus cloud. The Mueller matrix is a very important tool possibly giving more information about the medium. In this method multiple scattering was included.

In Case 1, the 4×4 Mueller matrix is displayed for a mixed habit cirrus cloud. This relationship between the Mueller matrix and scattering matrix elements are noted. Particularly, for first element, M_{11}, and the last element, M_{44}/M_{11}, the relationship is noticeable because of their invariance to the rotations of the reference plane. Of course in radiative transfer where polarization is neglected, M_{11} is the only element available. Therefore, polarization provides more information, available in the other elements of the Mueller matrix, where shape, size, optical depth, and other properties of the constituents that make up the cirrus cloud may be distinguished.

In Case 2, three different cirrus clouds of $\tau = 1$, each composed of a single habit were studied. The single-scattering Mueller matrix is found to be the best method for distinguishing characteristics between habits where the incident angle is $\theta = 0^\circ$. The

M_{12}/M_{11}, M_{13}/M_{11}, M_{42}/M_{11}, and M_{43}/M_{11} elements are all found to have great dependence on habit. Here M_{12}/M_{11} and M_{43}/M_{11} are studied in greater detail. The scattering element $-P_{12}/P_{11}$ is closely related to M_{12}/M_{11}. The features found in $-P_{12}/P_{11}$ are produced by rays that undergo specific internal reflections. For bullet rosette and aggregate, the peaks are less pronounced. This is possibly due to increased internal reflections through the branches of bullet rosette and the more complicated structure and rougher surface of aggregate.

The peaks found in M_{43}/M_{11} for plate are very distinct and have strong polarization. Bullet rosette is less distinct with smaller fluctuations. Aggregate appears quite smooth, showing more fluctuations, but not as amplified. These distinctions between these three habits, of such different structure possibly provide a means for determining ice crystals of complicated structure.

Finally, it is recognized that plate is negatively polarized for the M_{44}/M_{11} element. Neither bullet rosette nor aggregate show this feature. Combining M_{12}/M_{11}, M_{43}/M_{11}, and M_{44}/M_{11}, provide a way to distinguish between these three habits. Of course the idea is to use radiative transfer, where multiple scattering within a layer is occurring. This becomes a little more difficult because the peak features are lost as the optical depth increases. However, with more study of these elements for different scenarios and making use of all the elements, the possibility of determining the properties of a cirrus cloud using remote sensing will increase.

Case 3 was an attempt to make a distinction of effective sizes using the Mueller matrix. For the most part, there are very little differences in the scattering matrix elements between the three effective sizes for bullet rosette. The only major differences occur in the strength of the polarization found in some elements. Plate varied in the same manner as bullet rosette. However, aggregate provided not even a slight distinction between effective sizes. This is possibly a consequence of the rough surfaces of aggregate.

Despite, the lack of information provided by examining the effective sizes it must be understood that this comparison only looked at three effective sizes for a specific experiment in the middle latitudes. Size distributions for ice crystals range across the earth, from the polar latitudes to tropical latitudes. These size distributions are not completely representative. Also, the ice crystals are considered to be randomly oriented. It is believed that ice crystals that are oriented in a specific direction will provide more information regarding their size.

In Case 4, the depolarization ratios are defined and studied for the three habits, effective sizes and optical depths. The depolarization ratios are definitely dependent on the habit. The depolarization ratios are calculated using two different incident polarization states. A comparison of the habits is made, by combining the depolarization ratios using $\delta_h - \delta_v$. This method brings out the $-P_{12}/P_{11}$ element, which is quite different between the habits. Therefore, if $\delta_h - \delta_v$ is obtained from measurement and the $-P_{12}/P_{11}$ element is known than this is a very effective way to distinguish habits.

Again, an attempt was made to distinguish effective sizes by using the depolarization ratios. The $-P_{12}/P_{11}$ element does not vary much between these effective sizes and therefore the depolarization ratios do not vary much either. The $\delta_h - \delta_v$ method was used, but the only differences are found in the strengths of these two ratios compared to effective size.

For all habits, the depolarization ratio increases for increasing optical depth. The effect of increased multiple scattering, increases the depolarization ratio. This is due to increased reflections and increased rotations of the incident plane. Something else to consider, which I did not, is examining the properties using a different wavelength, for instance, near-infrared. This would provide more information about cirrus clouds and could be used along with that discussed above to obtain a better understanding of cirrus clouds. Yang and Liou,[40] concluded that results for polarization using an absorbing wavelength, $\lambda = 3.7\mu m$, vary greatly with size parameter. A greater distinction of the effective sizes is likely when using the near-infrared wavelength.

To better understand the role cirrus clouds have in the overall energy budget of our earth, the microphysical and optical properties of cirrus clouds must be accurately resolved. Using the polarization of light can help gain more information, distinguishing information, about cirrus clouds and their constituents. Using the visible wavelength, $\lambda = 0.532\mu m$, provides distinguishing information for habits. The Mueller matrix does not show much dependence on these three effective sizes for the visible wavelength. Finally, the depolarization ratio is quite dependent on the optical depth. Polarization

techniques such as the Mueller matrix and depolarization ratio provide a means for making these distinctions. Therefore, the Mueller matrix, by more observation, may provide much improved knowledge of the cirrus clouds we want to define.

REFERENCES

1. T. Nakajima and M. D. King, "Determination of the optical thickness and effective particle radius of clouds from reflected solar radiation measurements. Part I: Theory." J. Atmos. Sci. **47**, 1878-1893 (1990).
2. M. I. Mishchenko, W. B. Rossow, A. Macke, and A. A. Lacis, "Sensitivity of cirrus cloud albedo, bidirectional reflectance and optical thickness retrieval accuracy to ice particle shape," J. Geophys. Res. **101**, 16973-16985 (1996).
3. H-L. Huang, P. Yang, H. Wei, B. A. Baum, Y. Hu, P Antonelli, and S. A. Ackerman, "Inference of ice cloud properties from high spectral resolution infrared observations," IEEE Trans. Geosci. Rem. Sensing **42**, 842- 853 (2004).
4. K. N. Liou, "Influence of cirrus clouds on weather and climate processes: a global perspective," Monthly Weather Rev. **114**, 1167-1199 (1986).
5. A. J. Heymsfield, K. M. Miller, and J. D. Spinhirne, "The 27-28 October 1986 FIRE IFO cirrus case study: Cloud microstructure," Mon. Weather Rev. **188**, 2313-2328 (1990).
6. A. J. Heymsfield and C. M. R. Platt, "Parameterization of the particle size spectrum of ice clouds in term of the ambient temperature and ice water content," J. Atmos. Sci. **41**, 846-855 (1984).
7. A. J. Heymsfield and J. Iaquinta, "Cirrus crystal terminal velocities," J. Atmos. Sci. **57**, 916-938 (2000).

8. W. P. Arnott, Y. Y. Dong, J. Hallett, and M. R. Poellot, "Role of small ice crystals in radiative properties of cirrus: A case study, FIRE II, Novemeber 22, 1991," J. Geophys. Res. **99**, 1371-1381 (1994).
9. S. L. Nasiri, B. A. Baum, A. J. Heymsfield, P. Yang, M. R. Poellot, D. P. Kratz, and Y. Hu, "The development of midlatitude cirrus models or MODIS using FIRE-I, FIRE-II, and ARM in situ data," J. Appl. Meteor. **41**, 197-217 (2002).
10. G. G. Mace, E. E. Clothiaux, and T. P. Ackerman, "The composite characteristics of cirrus clouds: Bulk properties revealed by one year of continuous cloud radar data," J. Climate **14**, 2285-2203 (2001).
11. A. J. Heymsfield, "Cirrus uncinus generating cells and the evolution of cirriform clouds," J. Atmos. Sci. **32**, 799-808 (1975).
12. Q. Fu, "An accurate parameterization of the solar radiative properties of cirrus clouds for climate models," J. Climate **9**, 2058-2082 (1996).
13. D. L. Mitchell, S. K. Chai, Y. Liu, A. J. Heymsfield, and Y. Dong, "Modeling cirrus clouds. Part I: Treatment of bimodal size spectra and case study analysis," J. Atmos. Sci. **53**, 2952-2966 (1996).
14. B. A. Baum, D. P. Kratz, P. Yang, S. C. Ou, Y. Hu, P. F. Soulen, and S-C. Tsay, "Remote sensing of cloud properties using MODIS airborne simulator imagery during SUCCESS. Data and models," J. Geophys. Res. **105**, 11767-11780 (2000).
15. Q. Cai and K. N. Liou, "Polarized light scattering by hexagonal ice crystals: Theory," Applied Optics **21**, 3569-3580 (1982).

16. Y. Takano and K. N. Liou, "Radiative transfer in cirrus clouds. Part III: Light scattering by irregular ice crystals," J. Atmos. Sci. **52**, 818-837 (1995).

17. P. Yang and K. N. Liou, "Light scattering by hexagonal ice crystals: Comparison of finite-difference time domain and geometric optics models," J. Opt. Soc. Amer. A **12**, 162-176 (1995).

18. K. N. Liou, *An Introduction to Atmospheric Radiation* (Academic, London, 2002).

19. Y. Takano and K. N. Liou, "Solar radiative transfer in cirrus clouds. Part I: Single-scattering and optical properties of hexagonal ice crystals," J. Atmos. Sci. **46**, 3-19 (1989).

20. S. Chandrasekhar, *Radiative Transfer* (Dover, New York, 1960).

21. K. L. Coulson, J. V. Dave, and Z. Sekera, *Tables Related to Radiation Emerging from a Planetary Atmosphere with Rayleigh Scattering* (University of California, Berkeley, CA, 1960).

22. H. C. van de Hulst, *Multiple Light Scattering: Table, Formulas, and Applications* Vol. 1 (Academic, New York, 1980).

23. J. F. Haan, P. B. Bosma, and J. W. Hovenier, "The adding method for multiple scattering calculations of polarized light," Astron. Astrophys. **183**, 371-391 (1987).

24. G. G. Stokes, "On the composition and resolution of streams of polarized light from different sources," in *Polarized Light*, W. Swindell, ed. (Dowden, Hutchinson & Ross, Stroudsburg, PA, 1975), pp. 124-141.

25. S. Chandrasekhar, "On the radiative equilibrium of a stellar atmosphere. XV," Astrophys. J. **105**, 424 (1947).

26. J. Lenoble, *Radiative Transfer in Scattering and Absorbing Atmospheres: Standard Computational Procedures* (A. DEEPAK, Hampton, VA, 1985).

27. G. N. Plass and G. W. Kattawar, "Monte Carlo calculations of light scattering from clouds," Applied Optics **7**, 415-419 (1968).

28. H. H. Tynes, *Monte Carlo Solutions of the Radiative Transfer Equation for Scattering Systems* [Dissertation] (Texas A&M University, College Station, 2001).

29. J. D. Jackson, *Classical Electrodynamics*, 3rd ed. (Wiley & Sons, Inc., New York, 1998).

30. R. W. Ditchburn, *Light* (Dover, New York, 1991).

31. M. I. Mishchenko and L. D. Travis, "Maxwell's equations, electromagnetic waves, and Stokes parameters," in *Photpolarimetry in Remote Sensing*, G. Videen, Ya. Yatskiv, and M. Mishchenko, eds. (Kluew Academic Publishers, Dordrecht, The Netherlands, 2004), pp. 1-44.

32. R. T. Birge, "On the nature of unpolarized light," in *Polarized Light*, W. Swindell, ed. (Dowden, Hutchinson & Ross, Stroudsburg, PA, 1975), pp. 171-174.

33. J. E. Hansen and L. D. Travis, "Light scattering in planetary atmospheres," Space Sci. Rev. **16**, 527-610 (1974).

34. H. C. van de Hulst, *Light Scattering by Small Particles* (Dover, New York, 1981).

35. J. W. Hovenier, "Structure of a general pure Mueller matrix," Applied Optics **33**, 8318-8324 (1994).

36. A. H. Hielscher, A. A. Eick, J. R. Mourant, D. Shen, J. P. Freyer, and I. J. Bigio, "Diffuse backscattering Mueller matrices of highly scattering media," Optical Soc. Amer. **1**, 441-453 (1997).

37. J. W. Hovenier and C. V. M. van der Mee, "Fundamental relationship relevant to the transfer of polarized light in a scattering atmosphere," Astron. Astrophy. **128**, 1-16 (1983).

38. C. N. Adams and G. W. Kattawar, "Solutions of the equations of radiative transfer by an invariant imbedding approach," J. Quant. Spectrosc. Radiat. Transfer **10**, 341-356 (1970).

39. J. E. Hansen, "Multiples scattering of polarized light in planetary atmospheres. Part I. The doubling method," J. Atmos. Sci. **28**, 120-125 (1971).

40. P. Yang and K. N. Liou, "Geometric-optics-integral-equation method for light scattering by nonspherical ice crystals," Applied Optics **35**, 6568-6584 (1996).

41. P. Yang and K. N. Liou, " Light scattering by hexagonal ice crystals: solutions by a ray-by-ray integration algorithm," J. Opt. Soc. Amer. A **14**, 2278-2289 (1997).

42. P. Yang, B. C. Gao, B. A. Baum, Y. X. Hu, W. J. Wiscombe, S. Tsay, D. M. Winker, and S. L. Nasiri, "Radiative properties of cirrus clouds in the infrared

$(8-13\ \mu m)$ spectral region," J. Quant. Spectrosc. Radiat. Transfer **70**, 473-504 (2001).

43. J. W. Hovenier, "Symmetry relationships for scattering of polarized light in a slab of randomly oriented particles," J. Atmos. Sci. **26**, 488-499 (1969).
44. W. J. Wiscombe, "The Delta-M method: Rapid yet accurate radiative flux calculations for strongly asymmetric phase functions," J. Atmos. Sci. **34**, 1408-1422 (1977).
45. Y.-A. Hu, G. Wielicki, B. Lin, G. Gibson, S.-C. Tsay, K. Stamnes, and T. Wong, "δ-fit: A fast and accurate treatment of particle scattering phase functions with weighted singular-value decomposition least-squares fitting," J. Quant. Spectros. Radiat. Transfer **65**, 681-690 (2000).
46. M. Chami, R. Santer, and E. Dilligeard, "Radiative transfer model for the computation of radiance and polarization in an ocean-atmosphere system: polarization properties of suspended matter for remote sensing," Applied Optics **40**, 2398-2416 (2001).
47. Y. Takano and K. Jayaweera, "Scattering phase matrix for hexagonal ice crystals computed from ray optics," Applied Optics **24**, 3254-3263 (1985).
48. K. Sassen and K. N. Liou, "Scattering of polarized laser light by water droplet, mixed-phase and ice crystals. Part II: Angular depolarizing and multiple-scattering behavior," J Atmos. Sci. **36**, 852-861 (1979).

VITA

Ryan Lee Lawless received his Bachelor of Science degree in meteorology at Texas A&M University in College Station in May 2003. He continued in the atmospheric sciences program at Texas A&M University beginning in June 2003, and received his Master of Science degree in August 2005.

Mr. Lawless will continue to seek his PhD in the Biomedical Engineering Department at Texas A&M University beginning in September 2005. His research interests are radiative transfer and the polarization of light. He plans to publish a paper related to the topics discussed in this thesis.

Mr. Lawless may be reached at the Department of Atmospheric Sciences, Texas A&M University, 3150 TAMU, College Station, TX 77843-3150. His email address is ryan-lee-lawless@tamu.edu.